



LAWRENCE
LIVERMORE
NATIONAL
LABORATORY

Fiscal Year 2004 Summary Report: General Corrosion and Passive Film Stability

C. A. Orme, J. Gray, J. Hayes, L. Wong, R. Rebak, S.
Carroll, J. Harper, G. Gdowski

December 14, 2004

Disclaimer

This document was prepared as an account of work sponsored by an agency of the United States Government. Neither the United States Government nor the University of California nor any of their employees, makes any warranty, express or implied, or assumes any legal liability or responsibility for the accuracy, completeness, or usefulness of any information, apparatus, product, or process disclosed, or represents that its use would not infringe privately owned rights. Reference herein to any specific commercial product, process, or service by trade name, trademark, manufacturer, or otherwise, does not necessarily constitute or imply its endorsement, recommendation, or favoring by the United States Government or the University of California. The views and opinions of authors expressed herein do not necessarily state or reflect those of the United States Government or the University of California, and shall not be used for advertising or product endorsement purposes.

This work was performed under the auspices of the U.S. Department of Energy by University of California, Lawrence Livermore National Laboratory under Contract W-7405-Eng-48.

FY04 Summary Report: General Corrosion and Passive Film Stability

**Chris Orme¹, Jeremy Gray, Joel Hayes, Lana Wong, Raul Rebak, Susan Carroll,
Jennifer Harper, and Greg Gdowski**

Lawrence Livermore National Laboratory
Livermore, CA 94550

¹ Corresponding Author: orme1@llnl.gov

1. INTRODUCTION	3
2. GENERAL CORROSION OF ALLOY 22 FROM 60 TO 220°C	3
3. GENERAL CORROSION FROM WEIGHT-LOSS	4
ALLOY 22 AND TITANIUM LONG-TERM CORROSION FACILITY AT 60 AND 90C	4
<i>Methods</i>	4
<i>Results and Discussion</i>	5
Alloy 22	5
Ti grades 7, 12, and 16	8
ALLOY 22 CORROSION FROM 120 TO 220C	9
<i>Methods:</i>	10
Autoclave Capabilities	10
Environments	10
Weight-loss measurements	11
Surface Analysis Techniques	12
<i>Results and Discussion</i>	13
General Corrosion of Alloy 22 from 120 to 220C	13
Evaluation of surface oxides of autoclave samples	16
A comparison of surface compositions evaluated by XPS	16
A comparison between Brine solution with varying [NO ₃]/[Cl] ratio	21
<i>Implications to the General Corrosion Model</i>	27
4. CORROSION RATES IN CREVICE SOLUTIONS	29
CONNECTION TO CREVICE CORROSION MODELS	30
METHODS: TITRATION EXPERIMENTS	31
THE EFFECT OF ACID TYPE ON CORROSION	33
<i>Results and Discussion</i>	33
THE CORROSION INHIBITING EFFECTS OF NITRATES AND SULFATES ON ALLOY 22 IN ACIDIC ENVIRONMENTS	38
<i>Results and Discussion</i>	38
IMPLICATIONS TO ALLOY 22 CORROSION AT YUCCA MOUNTAIN	44
5. ACKNOWLEDGEMENTS	46
6. REFERENCES	47
<i>Documents Cited</i>	47
<i>Codes, Standards, and Regulations</i>	48
<i>N.5.3 Data, Listed by Data Tracking Number</i>	48

FY04 Summary Report: General Corrosion and Passive Film Stability

1. INTRODUCTION

This report summarizes both general corrosion Alloy 22 from 60 to 220°C and the stability of the passive film from 60 to 90°C over a range of solution compositions that are relevant to the in-drift chemical environment at the waste package surface. The general corrosion rates were determined by weightloss measurements in a range of complex solutions representing the evaporation of seepage water and more concentrated brines representing brines formed by the deliquescence of dust deposited on the canisters. These data represent the first weightloss measurements performed by the program at temperatures above 90°C. The low corrosion rates of Alloy 22 are attributed to the protective oxide film that forms at the metal surface. In this report, changes in the oxide composition are correlated with weightloss at the higher temperatures (140-220°C) where film characterization had not been previously performed. The stability of the oxide film was further analyzed by conducted a series of electrochemical tests in progressively more aggressive acid solutions to measure the general corrosion rates in solutions that mimic crevice or pit environments.

2. GENERAL CORROSION OF ALLOY 22 FROM 60 TO 220°C

The model for the general corrosion rate of Alloy 22 in the Yucca Mountain Repository Safety Analysis Report (BSC 2004a) is dependent on temperature, but independent of solution composition. The rate expression combines rate data derived from weightloss experiments conducted in LLNL Long Term Corrosion Test Facility and from rate data derived from short-term electrochemical tests. Both short-term and long-term data were combined, because these two independent studies showed contradictory results, where the long-term weightloss measurements are independent of temperature and the short-term electrochemical rates are dependent on temperature. The absence of temperature dependence in the long-term rates may be an artifact of the limited temperature range test (60 and 90°C), formation of carbonate and silica scales on coupons from the complex test solutions, and high uncertainty in the weightloss measurements. The inability to describe general corrosion rates as a function of solution composition may be an artifact of the limited number of and complexity of test solutions. Both the long-term weightloss and the short-term electrochemical experiments were conducted in modified sodium carbonate-type waters, in which important factors believed to inhibit localized corrosion such as NO₃ to Cl ratio are the same in all three solutions.

We conducted a series of autoclave experiments from 120 to 220°C with NO₃:Cl from 0.05 to 6.7 to provide more accurate representation of dependence of general Alloy 22 corrosion on temperature dependence and solution composition. In this study weightloss measurements were complemented by an array of surface analyses to measure the chemical composition, homogeneity, and thickness of the oxide layers to understand the role between passive film stability and net corrosion rate in these environments. These

environments are important to Yucca Mountain safety case, because recent dust deliquescent studies show that brines with high nitrate concentrations are likely to be stable at waste package surfaces at temperatures well above 150°C (Carroll et al., 2004).

Prior to reviewing the new general corrosion rate data from the autoclave and titration experiments, we review the Alloy 22 and Ti corrosion results from LLNL's Long Term Corrosion Test Facility that form the basis of general corrosion model (BSC 2004a,b).

3. GENERAL CORROSION FROM WEIGHT-LOSS

ALLOY 22 AND TITANIUM LONG-TERM CORROSION FACILITY AT 60 AND 90°C

General corrosion rates of Alloy 22 and Ti (grades 7, 12, and 16) were determined from weightloss measurements that had reacted with modified carbonate solutions over a five year period at 60 and 90°C. Details of these experiments are available in (Wong et al., 2003abc) and in DTN LL030412512251.057.

Methods

The corrosion rates of Alloy 22 and Ti (grades 7, 12, and 16) were determined using ASTM G 31 procedure for laboratory coupon immersion corrosion testing and ASTM G1 procedure for coupon preparation, cleaning and evaluation. Testing vessels were filled with about 1000 liters SDW, SCW, and SAW (Table 1), which were exposed to the ambient air. About half of the coupons were exposed to the liquid phase of the solution (complete immersion) and the other half were exposed to the vapor phase (suspended over the liquid surface). The coupons were exposed to the testing environments at their free corrosion potential (E_{corr}). Each coupon was electrically isolated from the other coupons. The reported test temperature corresponded to the liquid phase temperature. The exposure time for each coupon was approximately 5 years. Energy dispersive spectroscopy (EDS) and X-ray photoelectron spectroscopy (XPS) were performed on select coupons.

After a five-year exposure to each test solution, all 134 Alloy 22 and 382 Ti coupons were removed from their test vessels, rinsed with de-ionized (DI) water and stored in pre-labeled, individual containers. All coupons were then weighed three times at different times of the day to ensure complete removal of moisture. The coupons were cleaned prior to final weighing for the calculation of corrosion rates by weightloss, because they were covered with deposits. The cleaned surfaces were deposit-free and showed no noticeable corrosion in the tested electrolyte. All coupons tested in alkaline solutions (SCW and SDW) were cleaned per ASTM G 1–C6.1, which specifies cleaning with a HCl solution at ambient temperature. All coupons tested in an acidified solution (SAW) were cleaned per ASTM G 1 – C6.1 and C7.4, in which coupons were immersed in the HCl solution, rinsed in DI water, and immersed in hot (90-95°C) sodium hydroxide and potassium permanganate (NaOH/KMnO₄), and cleaned with diammonium citrate

((NH₄)₂HC₆H₅O₇) solution at ambient temperature. The corrosion rates of the cleaned coupons were then calculated using Equation 1,

$$CR \text{ (nm/yr)} = (8.76 \times 10^{10}) \Delta W / (\delta A t) \quad (1)$$

where 8.76×10^{10} is the proportionality constant, ΔW is the mass loss in grams after 5+ years, δ is the density (Alloy 22 = 8.69 g/cm³; Ti alloys = 4.52 g/cm³) A is the exposed surface area of each coupon (cm²) and t is the exposure time (hours). Corrosion rates for samples with crevices were calculated as general corrosion using equation 1, because no localized corrosion was observed. Thus samples labeled as “crevice” samples represent general corrosion only.

Results and Discussion

Alloy 22

Figure 1 and 2 plot weightloss corrosion rates for the Alloy 22 coupons exposed to the SAW, SCW and SDW solutions at 60°C and 90°C for over 5 years. Corrosion rates were similar for specimens reacted in different waters showing no temperature dependence. The individual corrosion rates for the weightloss coupons ranged from 0-23 nm/yr. This value is consistent with 20 nm/yr weightloss corrosion rates calculated for these waters after two years of reaction (Farmer et al., 2000). Stereomicroscopic and scanning electron microscope (SEM) observations of reacted specimens indicated little or no corrosion for Alloy 22, in which machining grooves remained uniform and sharp throughout each coupon. The averaged corrosion rate data from the 60°C experiments are used as input to the general corrosion model (BSC 2004a,b) as the temperature independent constant. This value was then coupled with the temperature dependence observed in short-term electrochemical systems in SAW to build the general corrosion rate model.

The modified carbonate waters were based on J-13 well water composition (Harrar et al., 1990) that was thought to be representative of the pore waters that would seep through the rock formations above the repository and onto the waste canisters. This study used three modifications of the well water to represent various extents of evaporation and acid conditions on the waste package. Two waters have pH(25°C) \approx 10 and are 10 times (SDW) and 1000 times (SCW) more concentrated than the J-13 well water. The third water represents a concentrated acid water (SAW), in which sulfuric, hydrochloric and/or nitric acid replace dissolved carbonate and lower the pH \approx 3 (25°C). Table 1. shows the measured major chemistry in these brines sampled at the 5 year period. Although NO₃ and Cl concentrations in these solutions are varied by 400 times and solution pH is acid or alkaline, the NO₃:Cl \approx 0.5 for most of the test solutions. It is possible that at these high NO₃:Cl, the NO₃ inhibits both local and general corrosion. It is also possible that the scale present on metal coupons served to protect Alloy 22 surfaces from the solutions and limit corrosion.

Table 1. Measured composition of corrosion solution after 5 years of reaction with test specimens in LLNL's Long Term Corrosion Test Facility

Sample ID	Soln. Type	pH @ 25°C	Chemical Composition, molal										
			Ca	Mg	Na	Si	K	TIC	F	Cl	NO3	SO4	NO ₃ /C
13-072904	SDW	9.58	0.00003	ND	0.02	0.0004	0.001	0.011	0.0007	0.002	0.001	0.002	0.53
14-072904	SDW	10.19	0.00003	ND	0.02	0.0015	0.001	0.004	0.0007	0.003	0.001	0.002	0.36
17-072904	SDW	9.59	ND	ND	0.01	0.0002	0.001	0.010	0.0006	0.002	0.012	0.002	7.39
22-072904	SDW	8.70	0.003	0.00005	0.02	0.0005	0.001	0.001	ND	0.003	0.004	0.002	1.31
23-072904	SDW	9.50	0.00003	ND	0.02	0.0001	0.001	0.010	0.0006	0.002	0.001	0.002	0.64
24-072904	SDW	10.15	ND	ND	0.02	0.0008	0.001	0.003	0.0016	0.003	0.001	0.002	0.19
29-072904	SDW	9.64	ND	ND	0.02	0.0002	0.001	0.009	0.0008	0.003	0.002	0.003	0.48
30-072904	SDW	8.37	0.001	0.001	0.02	ND	0.098	0.0002	ND	0.003	0.0001	0.002	0.03
09-072904	SCW	10.14	0.00004	ND	1.43	0.0018	0.076	0.686	0.069	0.196	0.110	0.129	0.56
10-072904	SCW	10.62	0.00006	ND	1.51	0.0006	0.091	0.586	0.076	0.188	0.106	0.123	0.57
11-072904	SCW	10.12	0.00005	ND	1.46	0.0015	0.091	0.611	0.067	0.191	0.106	0.123	0.55
12-072904	SCW	10.68	0.00006	ND	1.47	0.0006	0.090	0.551	0.080	0.195	0.108	0.128	0.56
20-072904	SCW	10.59	0.00007	ND	1.73	0.0019	0.091	0.659	0.070	0.200	0.113	0.131	0.56
21-072904	SCW	10.19	0.00003	0.00008	1.72	0.0002	0.091	0.588	0.032	0.205	0.101	0.191	0.49
27-072904	SCW	10.33	0.00007	ND	1.81	0.0018	0.092	0.630	0.064	0.199	0.116	0.129	0.58
28-072904	SCW	10.76	0.00006	ND	1.83	0.0038	0.092	0.511	0.074	0.211	0.119	0.138	0.56
25-072904	SAW	2.77	0.002	0.002	1.97	0.0011	0.102	0.000016	0.002	0.004	0.001	0.002	0.19
26-072904	SAW	3.88	0.002	0.002	1.95	0.0025	0.097	0.000005	ND	0.809	0.423	0.470	0.52

Source: DTN: LL041100112251.124

Corrosion Rate for 5+ Year LTCTF Samples - Alloy 22 Weight Loss Coupons

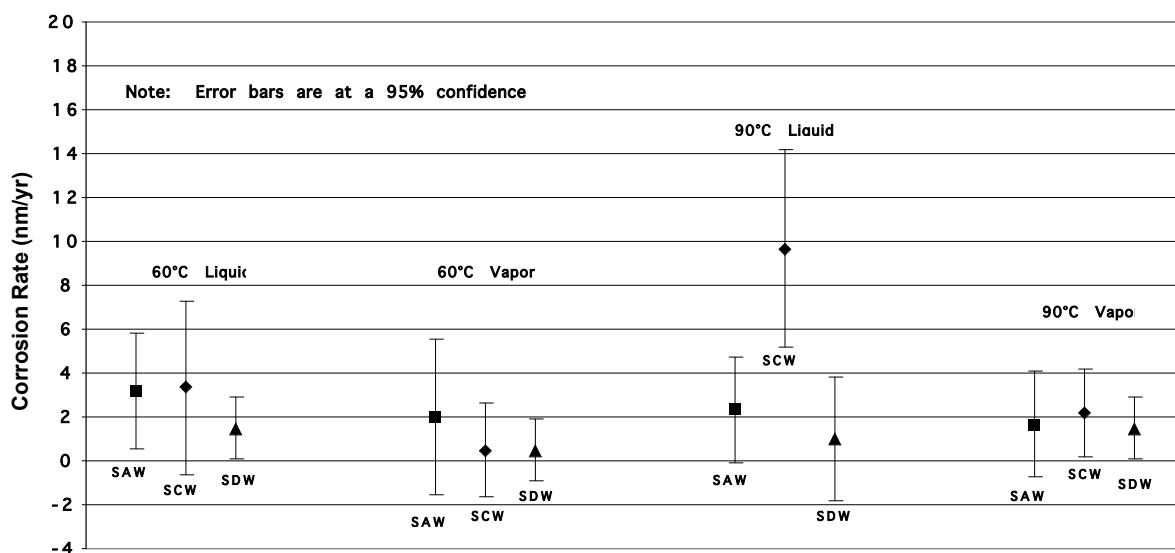


Figure 1. Corrosion Rates for Alloy 22 Weight Loss Coupons in SAW, SCW and SDW.

Corrosion Rate for 5+ Year LTCTF Samples - Alloy 22 Crevice Coupons

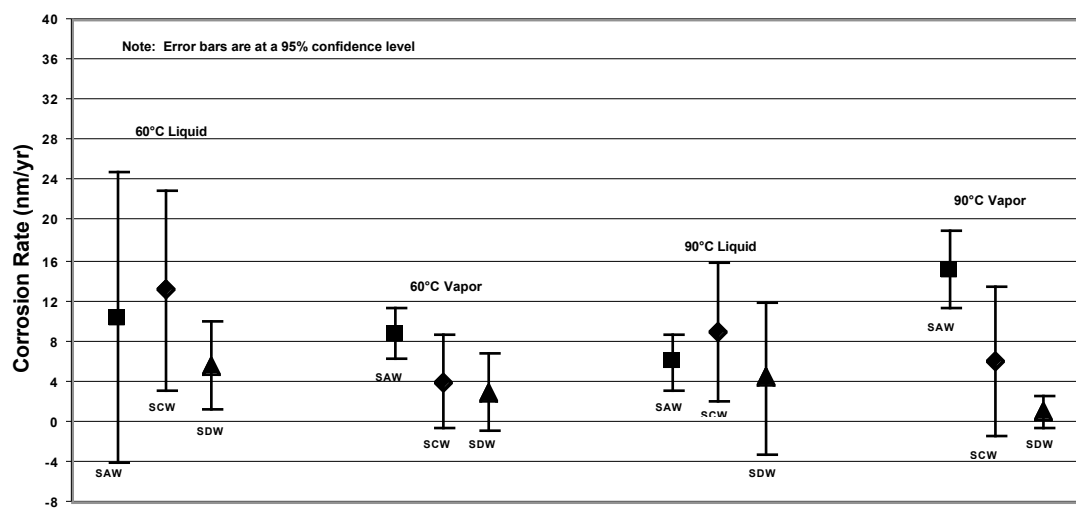


Figure 2. Corrosion Rates for Alloy 22 Crevice Coupons in SAW, SCW and SDW. These rates reflect general corrosion rates determined by weightloss, because no local corrosion was observed.

Ti grades 7, 12, and 16

In this section we briefly summarize general corrosion rates for Ti grade 7, 12, and 16 in SDW, SCW, and SAW solutions for a 2 to 5 year period. Ti grade 7 is the current alloy designated for drip shields above the waste packages. Figure 3 shows that Ti corrosion rates are dependent both on alloy grade and on temperature, where Ti grade 7 rates slower than Ti grade 16 rates, which are slower than Ti grade 12 rates. Rates of fully immersed coupons are about 5 to 10 times greater than coupons in the vapor phase, indicating greater water-surface interaction for the immersed samples. In contrast to the Alloy 22 samples, which exhibited constant corrosion rates, the observed temperature dependence indicates that scale precipitation did not isolate the metal surface from the solution. Rates are roughly 3 times higher at 90°C than at 60°C. Grade 7 rates increase from 8 to 31 nm/yr, grade 16 rates increase from 17 to 70 nm/yr and grade 12 rates increase from 71 to 201 nm/yr.

Corrosion rates also appear to be dependent on fluoride concentration, based on the 5 to 10 fold higher corrosion rates observed in SCW solutions than in SDW and SAW solutions (Figure 4). Fluoride concentrations in SCW are 100 times higher than in SDW and SAW. Ionic strength and pH cannot explain the differences, because SCW and SDW have similar pH, but very different corrosion rates. Similarly SAW and SCW have similar ionic strength, but very different corrosion rates.

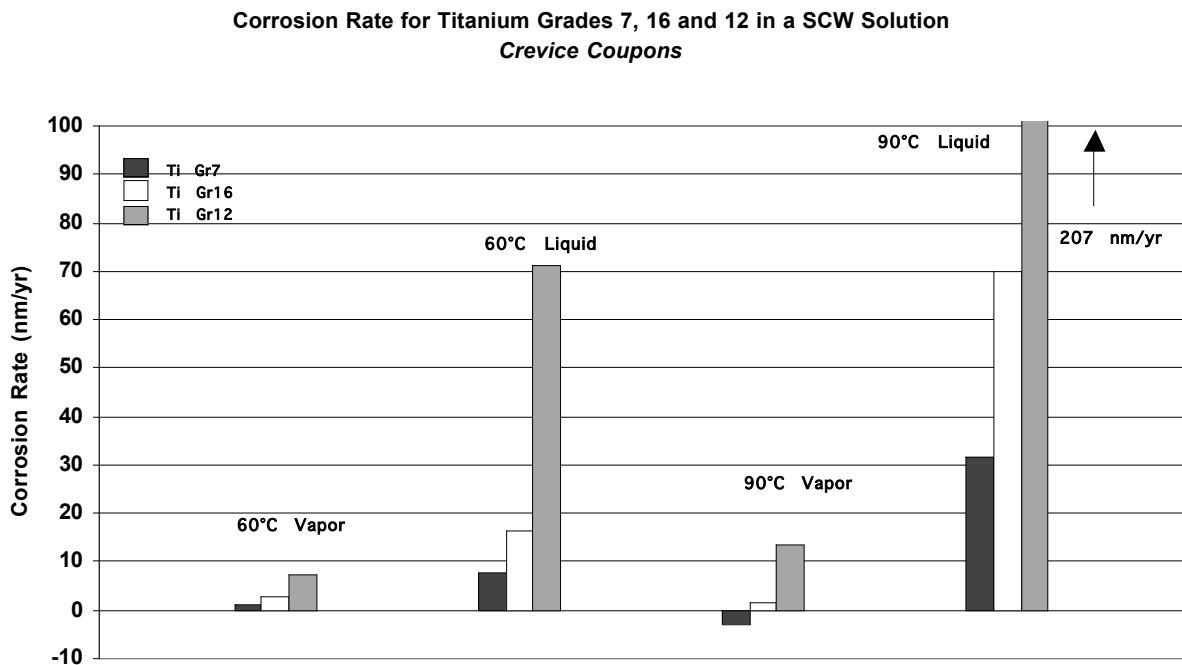


Figure 3. The effect of alloy composition on the corrosion rate of titanium alloys for crevice coupons immersed in a concentrated alkaline solution (SCW).

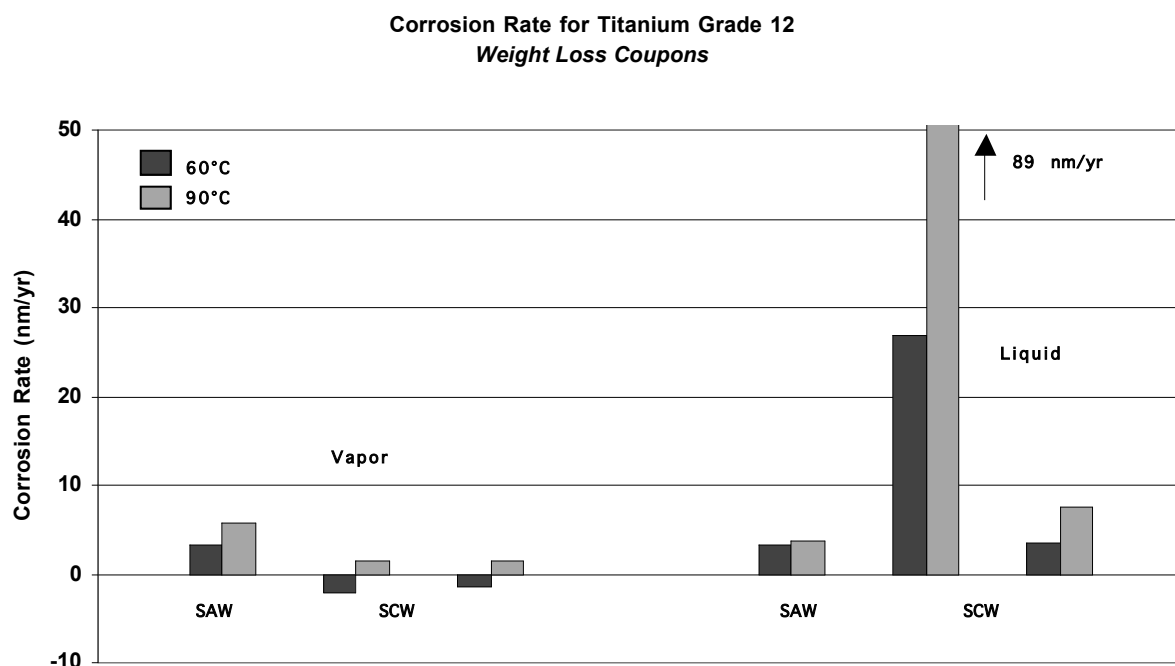


Figure 4. The effect of temperature on the corrosion rate of Ti Gr 12.

ALLOY 22 CORROSION FROM 120 TO 220C

The autoclave experiments fill a very important testing role for Yucca Mountain Project, because then can be used to evaluate the performance of Alloy 22 in concentrated brines at temperatures above 120 °C. Very little corrosion data exists at temperatures above 120 °C, and the data that has been collected are from electrochemical measurements. Weightloss measurements are a more accurate reflection of long-term corrosion, allowing natural oxide evolution and the formation of both anodic and cathodic regions on the alloy surface, which serves to decrease the general corrosion rate. Autoclaves not only allow weightloss studies to be conducted at elevated temperatures, but a properly designed experiment allows results to be obtained in as little as three months.

The objective of these experiments is to examine the influence of temperature and nitrate to chloride ratio on the corrosion rate of Alloy 22. These weightloss experiments differ from the Long Term Corrosion Test Facility experiments in three important ways. Firstly, the experiments are conducted over a much wider and higher temperature range. We anticipate that net corrosion rates at these higher temperatures will be above the detection limit of the weightloss technique such that a general corrosion model can be established from weightloss data alone. Secondly, the experiments are conducted in simple NaCl-NaNO₃-KNO₃ solutions compared to the complex modified carbonate waters used in the Long Term Corrosion Test Facility 5 year experiments. Therefore, no

carbonate and silica scale will form on the coupons. Thirdly, the solution $\text{NO}_3\text{:Cl}$ varies from 0.05 to 6.7 to examine the influence of nitrate/chloride ratio on the corrosion rate of Alloy 22. In particular, the ratio spans 0.2, which is sufficiently high to inhibit crevice corrosion in electrochemical tests. The range in absolute concentrations and relative $\text{NO}_3\text{:Cl}$ represent a range of solution compositions that might form at the waste package surface due to the evaporation of seepage or by the deliquescence of salts.

Methods:

Autoclave Capabilities

The autoclave facilities at LLNL include 3 autoclaves made from Hastelloy C-276, which is composed of the same elements as Alloy 22 (Figure 5a). This prevents foreign contamination of the solution through corrosion products from the canister walls; and, due to the high corrosion resistance of C-276, minimizes the amount of corrosion products entering the solution from the canister walls. A special sample holder was designed and fabricated out of Alloy 22, both to prevent contamination of the system and to eliminate any galvanic coupling (Figure 5b). These sample holders hold foil weight-loss samples as well as polished Alloy 22 pucks, which are used for surface analysis by Atomic Force Microscopy, Transmission Electron Microscopy, Auger Electron Spectroscopy, and X-ray Photoelectron Spectroscopy. All of the samples are held vertically to prevent precipitations from settling on the surface.

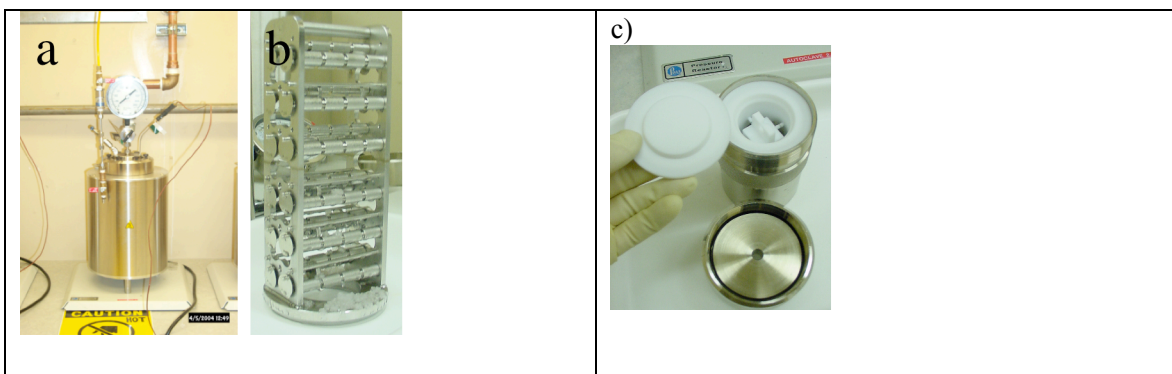


Figure 5 a) Autoclave setup, b) Alloy 22 sample holder for autoclave setup, and c) Teflon acid digestion bomb with Teflon sample holder inside.

The facility also consists of 8 Teflon Acid Digestion Bombs, capable of reaching temperatures of 175 °C with the samples held in an inert vessel (Figure 5c). Special Teflon sample holders were designed to hold the metal samples.

Environments

The solutions were high ionic strength brines composed of Na^+ , Cl^- , K^+ , and NO_3^- . The environments were designed to span the range of $\text{NO}_3^-/\text{Cl}^-$ ratios where crevice corrosion has been shown to initiate at 110°C. For practical reasons, the concentrations were chosen such that all salts were undersaturated at 90°C, allowing the fully mixed solutions

to be poured into the autoclaves. The solution ID's and the salt concentrations are shown in Table 2.

Table 2: Test solutions used in autoclaves and Teflon bombs.

Solution ID	NaCl (m)	NaNO ₃ (m)	KNO ₃ (m)	[NO ₃]/[Cl]	Total Molal
1	6.4	-	2.0	0.3125	8.4
2	2.7	3.4	15.1	6.7	21.2
3	6.4	-	0.3	0.05	6.7
4	6.4	-	3.2	0.5	9.6

Source: LL040502512251.099 and LL040907112251.122

Weight-loss measurements

A set of experiments have been performed at time intervals of 4 months and 9 months to examine the influence of temperature and nitrate/chloride ratio on the corrosion rate of Alloy 22. The details of the test are shown in the table 2. Weight-loss measurements were made in the environments marked as “4m” or “9m” at ~4-months and 9-months, respectively. The Teflon bombs held fewer samples and once opened all samples were removed. The larger volume of the autoclaves allowed samples to be removed at two times. The environments marked as “P” are experiments which are currently being initiated, and they will contain both weight-loss samples, polished pucks for oxide characterization, and foil crevice corrosion specimens to examine the influence of temperature and nitrate to chloride ratio on crevicing of Alloy 22. The foil crevice corrosion samples are our own invention and will simultaneously address the question of whether crevice corrosion will occur spontaneously in these environments as well as provide a direct measure of the difference in corrosion rate (as measured by weight-loss) for general and crevice corrosion under more realistic conditions where the process is not being driven electrochemically.

Table 3: Completed general corrosion tests

Solution		Temperature °C			
[NO ₃]/[Cl]	Total Molal	120	140	160	220
0.05	6.7		4m, 9m		
0.3125	8.4	4m	4m	4m	4m, 9m
0.5	9.6		4m, 9m		P
6.7	21.2	4m	4m	4m, P	P

¹ Entries indicate approximate duration of aging, 4-months or 9-months.

² Proposed experiments are marked as “P” and will also include crevice specimens.

Source: LL040502512251.099 and LL040907112251.122

The foil weights were measure at three time points: before they were introduced into the autoclave, immediately after removal from the autoclaves (after rinsing briefly with Millipore water to remove excess salts precipitating as the solution dried), and after a more extensive cleaning designed to remove the oxide (using procedures within ASTM-

G1-03 C.6.1). The cleaning method was developed and tested to clean the weight-loss specimens in the LTCTF (see section 2.1). The samples were cleaned in two solutions: 150 ml of 37% HCl: 1000 ml H₂O and 100 ml H₂SO₄: 1000 ml H₂O. After the samples were ultrasonicated in each cleaning solutions for 3 minutes they were rinsed with Millipore water (Orme 2004a). The weight-loss is the difference between the final weight after the cleaning procedure and the initial weight. The corrosion rate is determined from the weight-loss and the area of the specimen. A detailed error analysis was completed that accounts for the errors in weighing the specimens as well as the errors in measuring the area (LL040502512251.099 and LL040907112251.122). Our weighing facilities are capable of measuring weight changes to ± 0.00003 grams, which corresponds to 15 nm of metal loss over the area of the foil samples. Each environment contained 3-4 foil specimens. Because the standard deviation between these specimens was several orders of magnitude greater than the measurement error, it is this variation that is shown in the plots.

Surface Analysis Techniques

To characterize the three-dimensional composition of the oxide, several techniques were required. Surface sensitive techniques such as X-ray Photoelectron Spectroscopy (XPS) were used to evaluate the elemental composition and oxide stoichiometry over a large (mm²) area but from a narrow surface depth (nanometers). Auger electron spectroscopy measures elemental composition from a range of areas (nm² to mm²) with similar depth resolution. Both of these techniques can be used to create depth profiles due to their fine depth resolution however in this report we utilize only Auger depth profiling. Cross-sectional Transmission electron microscopy provides the structure, layering, thickness, and degree of crystallinity of the oxide layer but from a limited area of the surface. Electron energy loss spectroscopy (EELS), within the TEM, provides non-quantitative elemental maps. Atomic force microscopy is used to obtain surface topographic maps with lateral range $\sim 100\mu\text{m}$ and height resolutions of 0.1nm.

X-ray photoelectron spectroscopy (XPS) is a surface-sensitive analysis method used to determine the elemental composition and the chemical state of oxides formed on Alloy 22 coupons. Photoelectrons are generated within the X-ray penetration depth (typically many microns), but only the photoelectrons within the top three-photoelectron escape depths are detected. Escape depths are on the order of 15-35 Å, which leads to an analysis depth of $\sim 50\text{-}100$ Å. Typically, 95% of the signal originates from within this depth. All XPS measurements were performed on a PHI Quantum 2000 Quantum Scanning ESCA Microprobe using a monochromatic Al K_a source with photon energy 1486.6 electron volts (eV). The analysis area was 1400 μm x 300 μm . Spectra were charge corrected by aligning the chromium Cr2p₃ peak at 577.0 eV or the Carbon C1s peak at 284.8 eV.

Cross-sectional views of the metal-oxide interface were obtained using transmission electron microscopy (TEM). Samples were prepared using a focused ion beam “pluck out” method. Before the focused ion beam is used, a layer of gold-palladium is evaporated on to the surface to protect the oxide from beam damage during sample preparation. A much thicker platinum coating is then deposited using ion-assisted

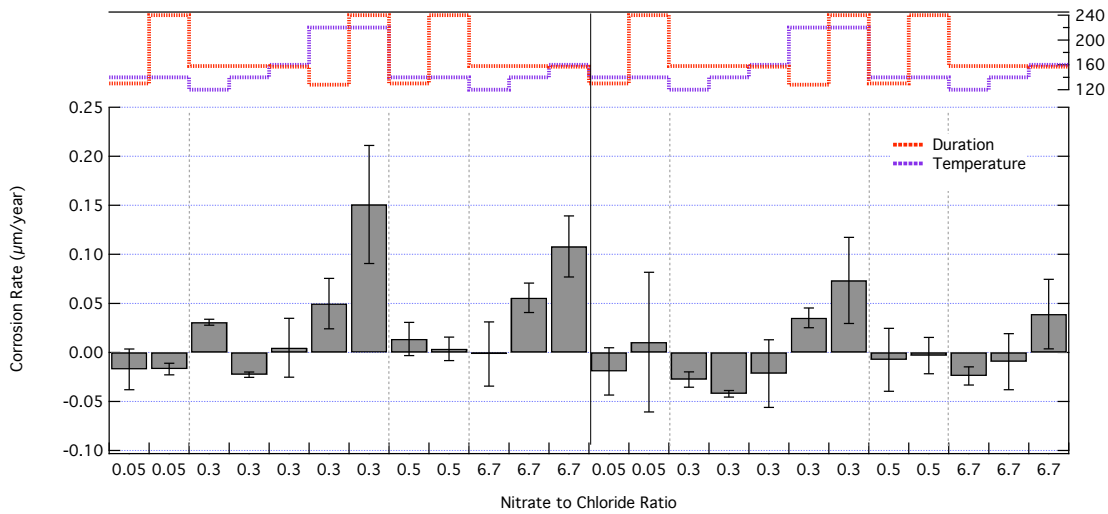
deposition. Both the Au-Pd and Pt layers can be seen in the TEM images. The Au-Pd layer, which appears dark in the bright field images shown below, can be used to mark the outer boundary of the oxide. Bright field images were obtained using a FEI-Philips TEM Model CM300FEG. Images display general oxide structure and can be used to quantify oxide thickness. Samples are typically 3 μ m long and images are obtained along the entire length of the sample. Images can also be correlated with elemental maps. All images shown in this report can be found in SN-LLNL-SCI-465-V5 (Orme 2004b).

Auger depth profiling was used to obtain elemental composition across the oxide metal interface. All Auger measurements were performed using a PHI 680 scanning Auger microprobe. Depth profiles were obtained by alternating an acquisition cycle with a sputter cycle. During the acquisition cycle selected elemental peak intensities were collected. The sputter cycle removed material from the surface of the sample using a 5keV Ar⁺ source rastered over a 3mm x 3mm area. In order to eliminate crater wall effects, the data were acquired from a smaller region in the center of the sputtered area. The depth profiles acquired show the etch time as x-axis. The ion gun conditions were chosen with an etch rate of 2.4nm/min in a thermally grown silicon dioxide (SiO₂ equivalent depths). Different materials will etch at different rates dependent on surface topography, crystallographic orientation, and incident ion beam angle. Actual depths in these materials could not be provided.

Results and Discussion

General Corrosion of Alloy 22 from 120 to 220C

Figure 6 shows general corrosion determined by weightloss measurements from all autoclaves and bombs as a function of nitrate to chloride ratio, temperature, and duration, for samples held in the solution and vapor phases. . The major finding is that all corrosion rates are significantly less than 0.25 micron per year for all temperatures and environments tested. Macroscopically, rates appear to increase at higher temperature and at the highest nitrate to chloride ratios. However, quantification of the observed trends is limited, because incomplete removal of oxide layers during the cleaning yields negative corrosion rates at temperatures at or below 140C. As a whole, the samples held in solutions had slightly higher corrosion rates than those held in vapor. Duration of experiment generally yielded similar corrosion rates, with the exception of samples held at 220 °C in solutions with [NO₃⁻]/[Cl⁻] =0.3, in which the corrosion rates increase with duration for both the solution and vapor environments.



Source: LL040502512251.099 and LL040907112251.122.

Note: The temperature (°C) and duration (days) are plotted at the top with a shared axis on the right hand side of the graph. Each measurement is an average of 3-6 different samples. The error bars represent the standard deviations in these measurements.

Figure 6. Corrosion rates for autoclave samples plotted as a function of nitrate to chloride ratio for samples held in the solution (left hand side of solid black line) and vapor (right hand side of solid black line).

We use the Arrhenius rate law to quantify the temperature dependence of Alloy 22 from our weight-loss experiments (Figure 7). Application of the Arrhenius rate law to corrosion yields a net activation barrier for metal to transform to oxide or aqueous ion:

$$R = R_0 e^{-E/kT},$$

where R_0 is the attempt frequency, E is the net activation barrier (kJ/mol), k is Boltzmann's factor, and T is the temperature (K). This yields an $E = 10.9 \pm 3.1$ kJ/mol, when we combine all positive rates regardless of NO_3/Cl ratio, which is lower than the value ($E = 25$ kJ/mol) used in the current generalized corrosion model (BSC, 2004a) based on the temperature dependence of short-term electrochemical tests.

Table 4. Corrosion Rate (CR) Versus Temperature (T) for Data in Figure 13.

NO_3/Cl	T (C)	T (K)	CR ($\mu\text{m}/\text{year}$)	σ_{CR}^1 ($\mu\text{m}/\text{year}$)	$\ln(\text{CR})^2$	Error ³ (σ_{CR}/CR)	N_A/kT^4 (mol/kJ)
0.3125	120	393.2	0.031	0.003	-3.479	0.099	0.31
0.3125	140	413.2	-0.023	0.003		-0.119	0.29
0.3125	160	433.2	0.005	0.030	-5.339	6.242	0.28
0.3125	220	493.2	0.050	0.026	-3.001	0.518	0.24
6.7	120	393.2	-0.002	0.033		-20.323	0.31

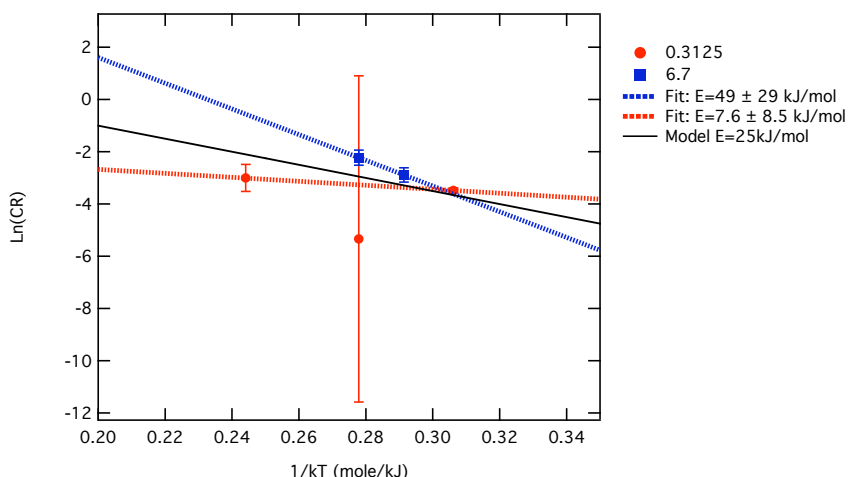
6.7	140	413.2	0.056	0.015	-2.887	0.271	0.29
6.7	160	433.2	0.108	0.031	-2.225	0.288	0.28

¹ Standard deviation of the corrosion rate

² Natural log of the corrosion rate. The log of a negative number is undefined and was left blank in the table for the two points with weight gains.

³ The propagated error for $\ln(CR)$ is σ_{CR} / CR

⁴ N_a is Avagadro's number (6.022×10^{23} atoms/mole), k is Boltzmann's constant (1.380×10^{-26} kJ/K), and T is temperature in Kelvin



Source:

Note: The y-axis is the natural log of the corrosion rate. The x-axis is N_a/kT where N_a is Avagadro's number (6.022×10^{23} atoms/mole), k is Boltzmann's constant (1.380×10^{-26} kJ/K), and T is temperature in Kelvin. The best line fit uses the values as well as the standard deviations to fit the line. The large uncertainty in the slopes (or activation energy) is due to the limited number of points (2 or 3). The corrosion rate data for NO_3/Cl of 0.3125 (red), which is representative of samples with a Cr_2O_3 barrier layer, has an activation barrier of 8 ± 8 kJ/mol. This is less than the 25kJ/mole (black line) that is used in YMP's general corrosion model. A separate fit was performed on the environment with NO_3/Cl of 6.7 because the surface composition analysis suggests a different dissolution mechanism. An activation barrier of 49 ± 29 kJ/mol is calculated for these data. However, more than two points and a temperature spread of more than 20C are required to have a more certain value.

Figure 7. Arrhenius Plot Displaying Corrosion Rate Data for Samples Held in Solutions with Nitrate to Chloride Ratio of 0.3125 (red) and 6.7 (blue).

As expected from an Arrhenius rate law, the highest corrosion rates (both for samples held in solution and in the vapor) were found at 220°C. Less intuitively, the second highest corrosion rates were observed in environments with the highest nitrate to chloride ratio, 6.7. This last case requires some explanation, because nitrate is often considered a corrosion inhibitor. If we consider only the $\text{NO}_3/\text{Cl} = 6.7$ rate data, then the $E = 49 \pm 29$ kJ/mol. Note that this value is based on two rates separated by only 20°C (one point was not used because it showed a weight gain). Both the change in activation barrier and the higher corrosion rates can be understood by looking at the surface composition data.

Evaluation of surface oxides of autoclave samples

In this section we describe the results of various surface analysis techniques to characterize surface film composition (XPS), the structure and thickness of the surface oxide (cross-sectional TEM) and composition through the oxide film (Auger depth profiling) formed on Alloy 22 when reacted in the solution and vapor for 4 and 9 months with NO_3/Cl ratios of 0.05 to 6.7 and with temperatures 120 to 220°C. Unlike the weight-loss specimens, these samples were only rinsed with Millipore water, and represent the surface state prior to cleaning.

A comparison of surface compositions evaluated by XPS

X-ray Photoelectron Spectroscopy (XPS) was used to evaluate the elemental composition and oxide stoichiometry at the outermost surface film as a function of the atomic % of the Alloy 22 constituents (Ni, Cr, Mo, W, Fe) for all of the reacted Alloy 22 foils (Table 4 and Figure 7).

Table 5. Autoclaved samples evaluated by XPS.

Sample	T (°C)	NO_3/Cl	Days	Envir. ^a	Ni oxide	Cr oxide	Fe ^b oxide	Mo oxide	W oxide	Ni/Cr oxide
DEA1046	140	0.05	130	3L	73.7	19	4	3	0.3	3.9
DEA 700	140	0.05	240	3L	41.8	43.2	7.5	6.8	0.7	1.0
DEA702	120	0.3125	158	1L	94.5	5	-	0.4	0.1	18.9
DEA701	140	0.3125	158	1L	81.7	13.7	4.4	0.2	-	6.0
JE1367	160	0.3125	157	1L	94.7	3	0.8	1	0.5	31.6
DEA1183	220	0.3125	128	1L	90.7	3	5.9	0.4	<0.1	30.2
DEA 1137	220	0.3125	240	1L	86	11.6	2.3	0.1	-	7.4
DEA1015	140	0.5	130	4L	84.1	8.4	6.4	1.2	-	10.0
JE 1328	140	0.5	240	4L	74.5	18.7	4.5	2.1	0.1	4.0
DEA687	120	6.7	158	2L	79.3	18.2	1.5	0.8	0.2	4.4
JE1317	140	6.7	158	2L	88.7	8.5	2.1	0.6	0.1	10.4
JE1375	160	6.7	157	2L	83.9	7.3	-	8.7	0.1	11.5
DEA1132	140	0.05	130	3V	74.2	14.4	5.9	5.1	0.4	5.2
DEA 706	140	0.05	240	3V	79.7	10.4	6.1	3.6	0.3	7.7
JE1331	120	0.3125	158	1V	71.3	15.1	6.3	6.9	0.4	4.7
DEA714	140	0.3125	158	1V	70	14.4	8.2	6.8	0.6	4.9
DEA1058	160	0.3125	157	1V	86.6	10.3	2.1	1	-	8.4
JE1306	220	0.3125	128	1V	78.9	17.7	1.8	1.7	-	4.5
JE 1372	220	0.3125	240	1V	83.4	14.2	1.5	0.8	<0.1	5.9
DEA1181	140	0.5	130	4V	69.8	16.4	7.7	5.4	0.7	4.3
DEA 1007	140	0.5	240	4V	75.3	11.4	8.7	4.4	0.3	6.6
JE1343	120	6.7	158	2V	26	43.6	14.1	14.8	1.5	0.6
DEA712	140	6.7	158	2V	80	15.9	3	0.9	0.2	5.0
JE1352	160	6.7	157	2V	84.4	11	-	4.6	<0.1	7.7

^a Solution number as detailed in Table 2. "L" and "V" indicate that the sample was held in the liquid phase or the vapor phase, respectively.

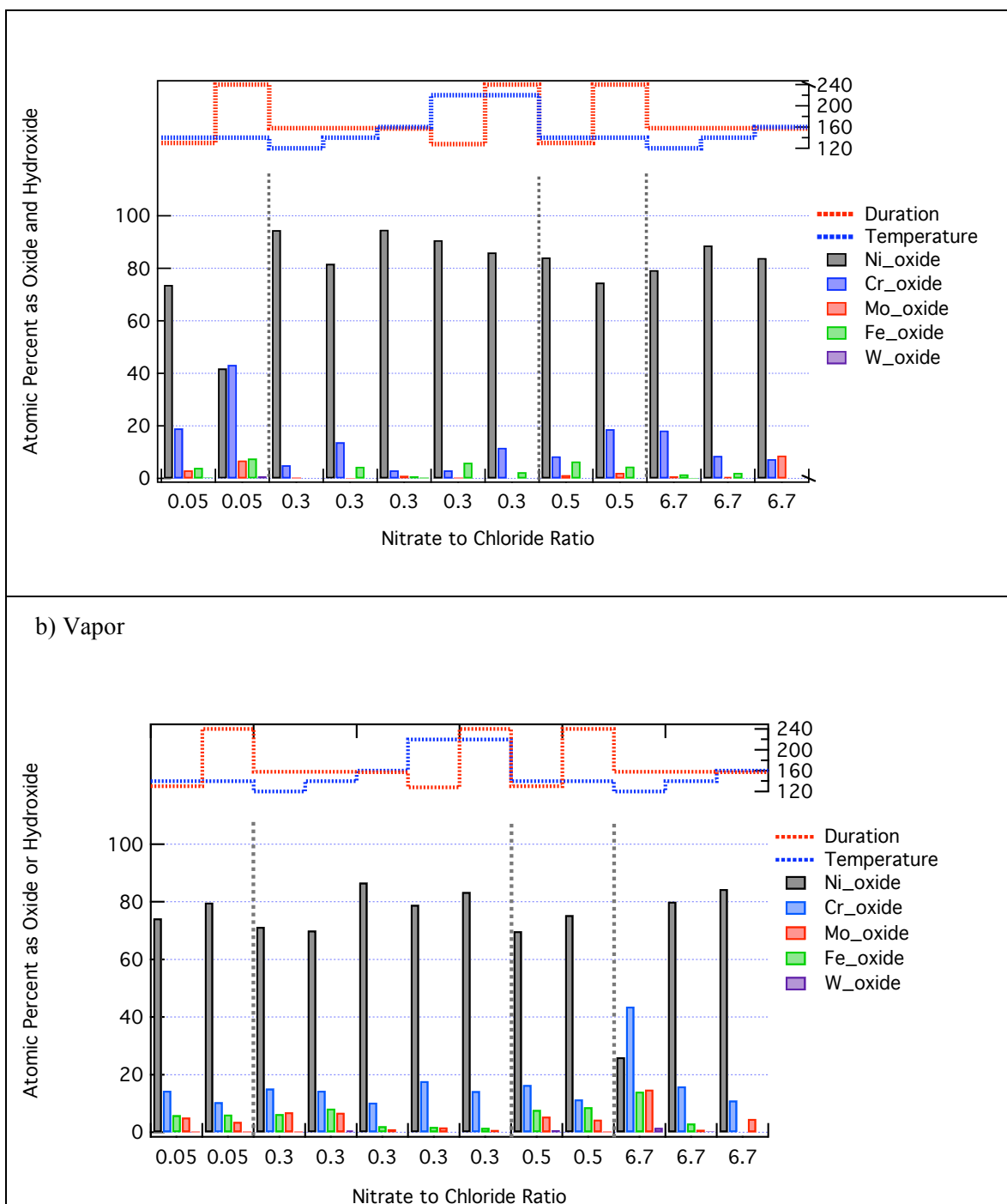
^b For the purposes of this calculation all detected Fe was assumed to be in the form of oxides.

Source: LLNL 2004a and LLNL 2004a

Curve fits of individual high-resolution spectra were used to distinguish contributions from metal, oxides, and hydroxides. Figure 7 displays the composition of the surface oxide and/or hydroxide after the metallic contribution was removed. Identical to the weightloss data, the XPS results are graphed by nitrate to chloride ratio, temperature and duration for both the solution and vapor phase studies. With the exception of two samples (DEA700 and JE1343) all of the specimens had a surface oxide primarily composed of Ni(OH)_2 , (70-95%) followed by various chromium oxides (3-19%). On most samples significantly lower and varying levels of molybdenum oxide, primarily as MoO_3 (or molybdate) were also found. Most, but not all, of the samples had low levels of Fe (presumably as an oxide) and trace levels of W.

The vapor and solution data sets have two subtle differences: 1) samples held in the vapor phase contain significantly more molybdenum oxide than those held in solution and 2) the Nickel/Chromium ratio in the oxide decreases with aging time for samples held in solution but increases with aging time for those held in vapor. Difference between the vapor and solution specimens result because the vapor specimens react with a thin film of fluid whereas solution specimens react with a large volume of liquid. Aside from possible differences in pH or salt concentrations, which we view as unlikely due to the high humidity, the vapor samples do not have a pathway for dissolving low solubility metal ions. Recalling that the observed oxides are a competition between formation from the base metal and dissolution at the oxide-solution interface, we hypothesize that the vapor oxides represent the case where the dissolution kinetics are very slow compared to samples held in solution. This interpretation suggests that molybdenum oxides form in both solution and vapor environments but dissolve out of the oxide when a solution pathway is present. Similarly the nickel to chromium ratio can be interpreted as higher Nickel solubility in solution. Analyzing the solutions could test these hypotheses.

a) Solution

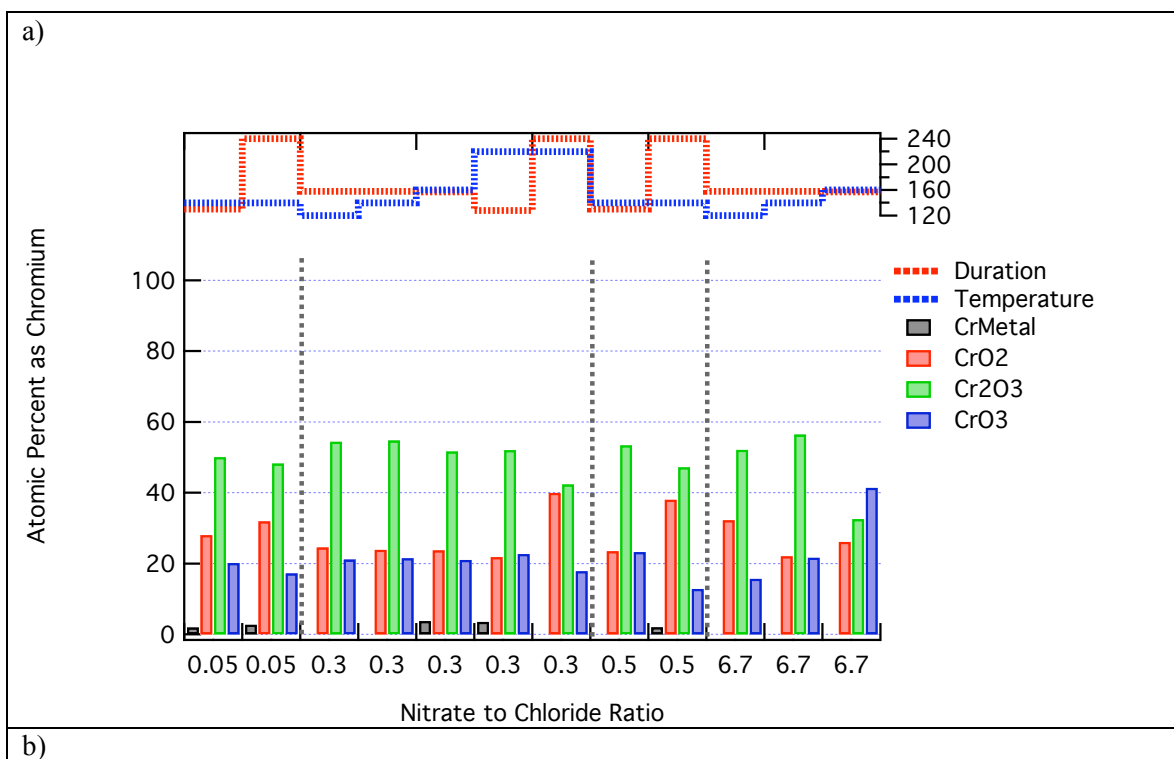


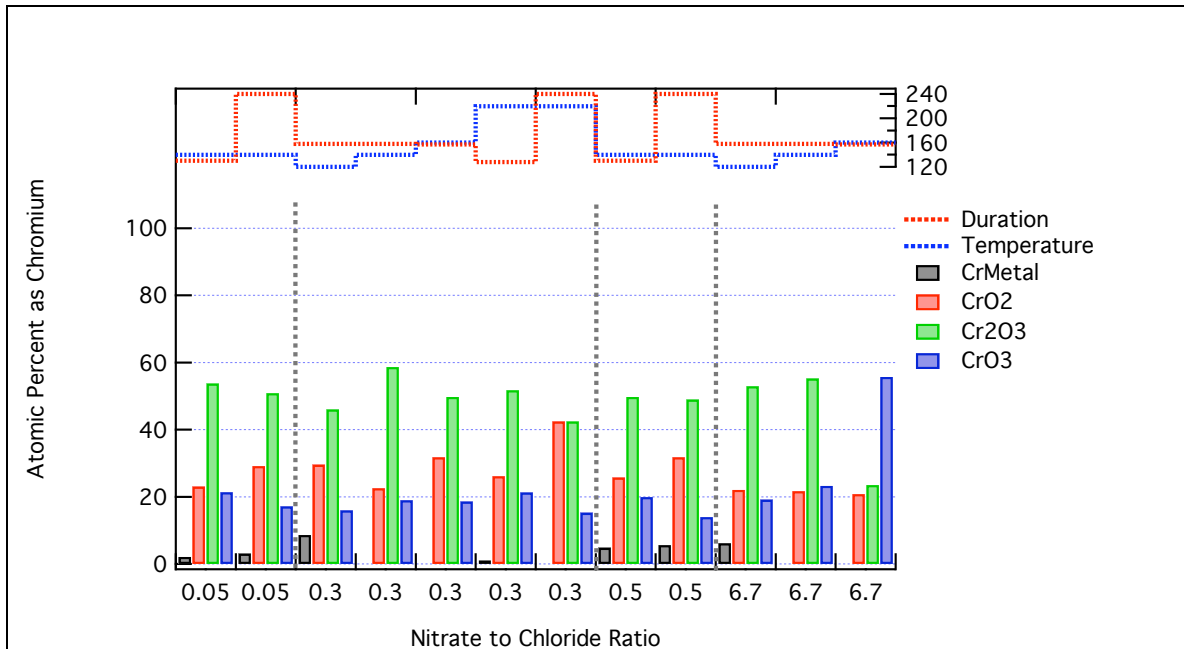
Source: MOL.20041015.0104 and MOL.20041007.0076

Note: The aging duration (days) and temperature (°C) are plotted at the top. Vertical dashed lines mark transitions in solution compositions. Samples were aged in a) solution, and b) vapor.

Figure 8. Atomic % of metal ions (Ni, Cr, Mo, Fe, W) as oxides or hydroxides displayed as a function of nitrate to chlorine ratio for 24 samples aged in autoclaves and analyzed by XPS.

Chromium speciation at the surface (Figure 8) was determined by fitting the chromium high-resolution spectra with four peaks associated with the different oxidation states: 0, for metal, +3 as found in Cr_2O_3 , $\text{Cr}(\text{OH})_3$, or CrOOH , +4 as found in CrO_2 , and +6 as found in CrO_3 . The model chosen uses the minimum number of peaks which is a virtue but may not be correct; more complex models will result in different quantification of the oxidation states. For all but two specimens (JE1375 and JE1352) chromium is predominately in the +3 oxidation state with a chromium spectra similar to that found for electrochemically grown passive oxide films formed at 90°C under a variety of electrolyte conditions (BSC 2004c). However at the highest NO_3/Cl ratio of 6.7 and 160°C , Cr(VI) becomes the dominant the surface chromium. High weightloss rates coupled with change in chromium speciation suggests that at higher temperatures, high nitrate:chloride accelerates the oxidation of the metal. As discussed above, the higher Cr(VI) levels in the vapor sample likely results from limited dissolution kinetics in thin films despite the high solubility of Cr(VI) oxides.





Source: MOL.20041015.0104 and MOL.20041007.0076

Note: The aging duration (days) and temperature ($^{\circ}\text{C}$) are plotted at the top. Vertical dashed lines mark transitions in solution compositions. Samples were aged in a) solution, and b) vapor.

Figure 9. The chromium composition at the surface of samples aged in autoclaves.

A comparison between Brine solution with varying [NO₃]/[Cl] ratio

More detailed surface analysis was performed on a subset Alloy 22 samples, because the XPS analysis discussed above only provides compositional information for the outermost surface of the oxide (within a few escape depths of the surface). We combine cross-sectional TEM and Auger depth profiling to compare oxide morphology, composition, and thickness as a function of aging time and brine environment (Table 5).

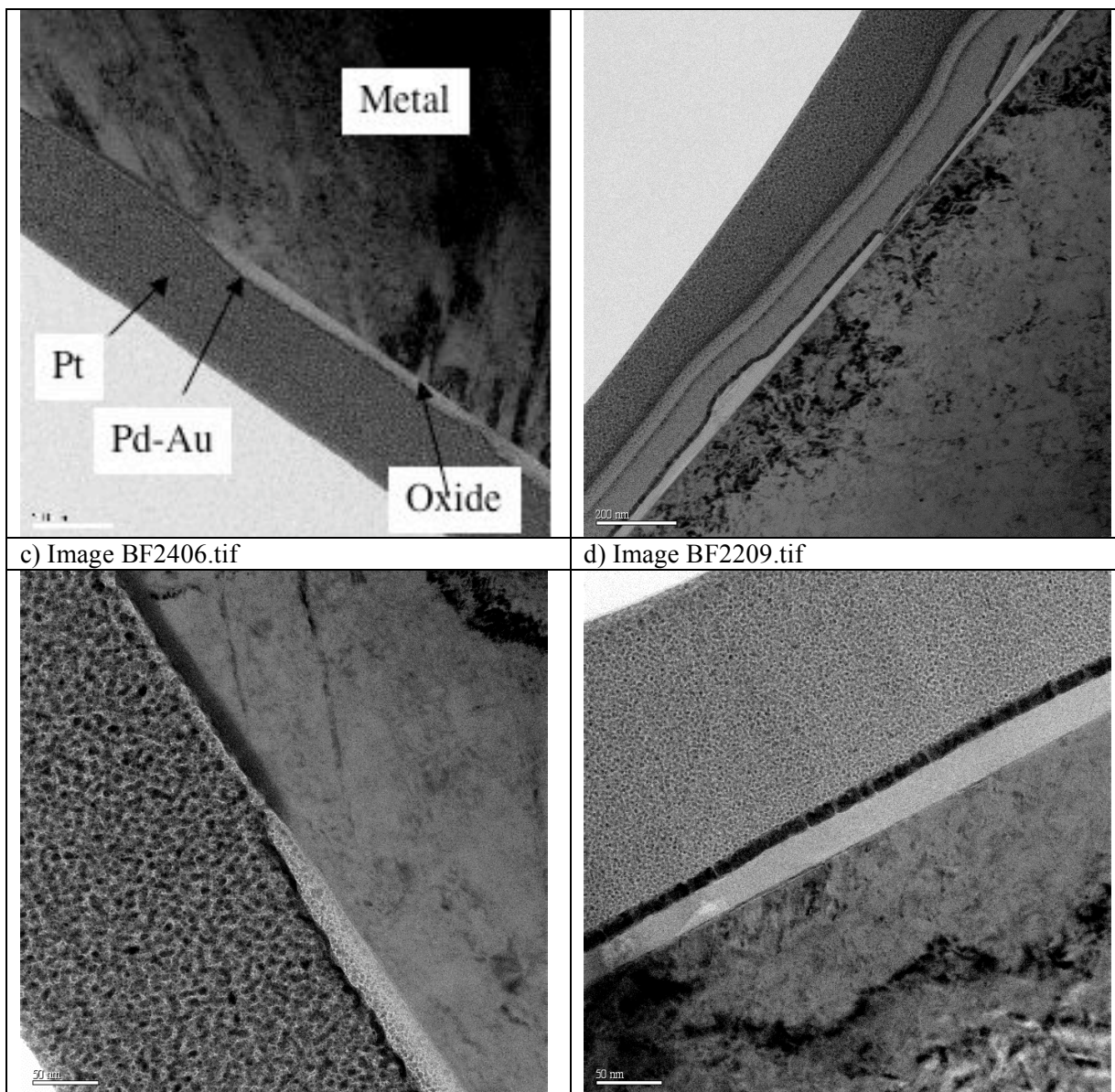
Table 6 Summarizes the environmental conditions and the identification numbers of autoclaved samples evaluated by XPS, Auger, and TEM

Temperature (°C)	[NO ₃]/[Cl]	Liquid/Vapor	Duration (days)	XPS Sample ID	Auger Sample ID	TEM Sample ID
140	0.05	Liquid	130	DEA1046	DEA1046	DEA1046
140	0.05	Liquid	240	DEA 700	DEA 700	DEA1041
140	0.5	Liquid	130	DEA1015	DEA1015	
140	0.5	Liquid	240	JE 1328	JE 1328	DEA1127
220	0.3125	Liquid	128	DEA1183	DEA1183	
220	0.3125	Liquid	240	DEA 1137	DEA 1137	DEA686

Source: Orme 2004b,

Comparison of cross-sectional TEM images for Alloy 22 reacted at 140°C in NO₃:Cl = 0.05 and 0.5 showed similar morphology and oxide thickness. Figures 9 and 10 shows cross-sectional views of the oxide at two magnifications for the samples aged 4-month and 9-months. The base-metal, oxide, Pd-Au layer, and one or more platinum layers are marked in figure 3a and are representative of all images shown in this report. The Pd-Au and platinum are due to the sample preparation process. The oxide is a light layer bounded by the thin, dark Au-Pd layer and the base-metal.

a) image BF2402.tif	b) Image BF2203.tif
---------------------	---------------------



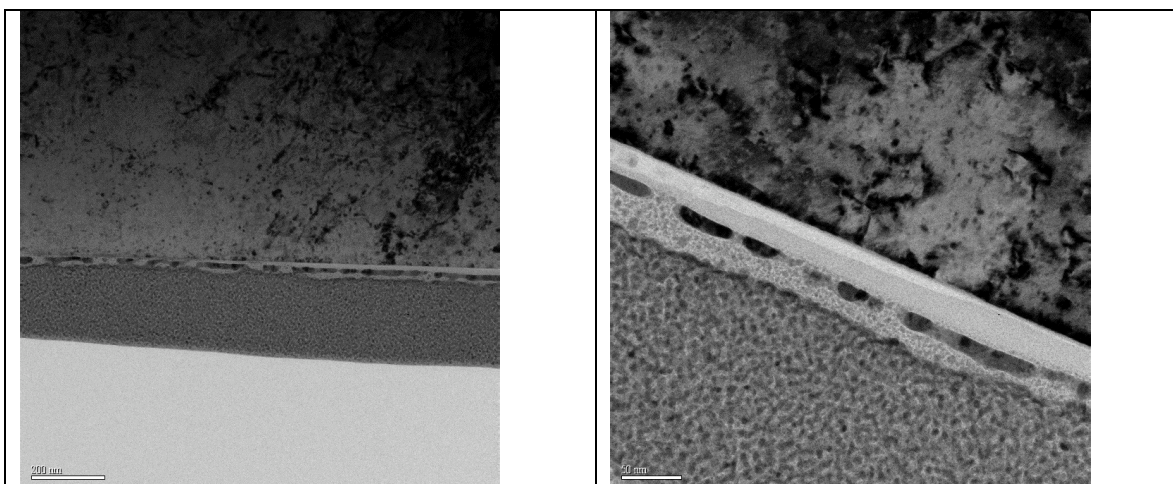
Source: Images from SN-LLNL-SCI-465-V5, Orme, 2004b.

Note: a,c) Sample DEA1046, aged ~4-months. The base metal is at the upper-right part of the image. The oxide is the wavy, light region next to the base metal. b,d) Sample DEA1041, aged ~9-months. The base-metal is in the lower-right portion of the image. The oxide is the wavy, light region next to the base-metal. a-b) A comparison of the surfaces at 17.5kx magnification. The scale bar is 200nm for both images.

c-d) A comparison of the surfaces at 65kx magnification. The scale bar is 50nm for both images.

Figure 10. Comparison between 4 months and 9 months of immersion in 140C brine with $\text{NO}_3/\text{Cl}=0.05$.

a)	b)
----	----



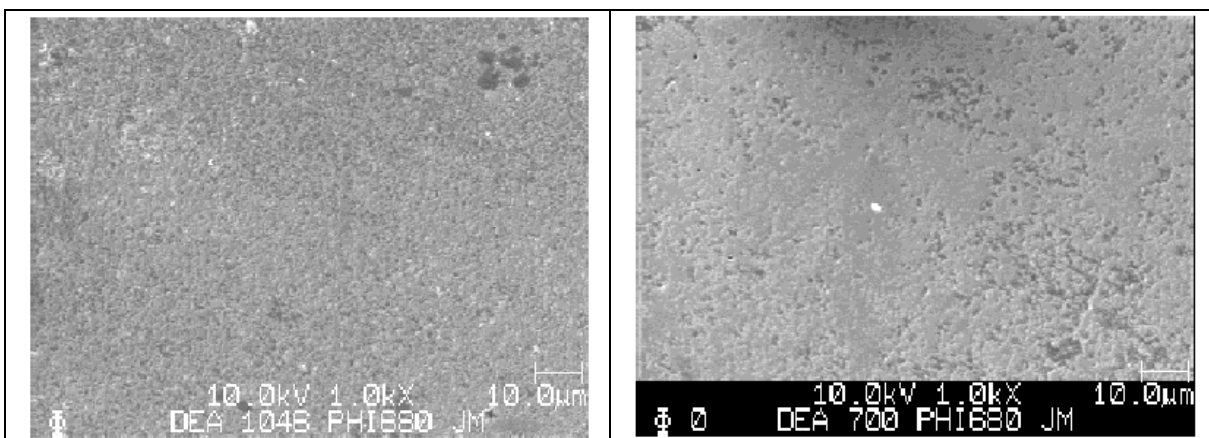
Source: Images from SN-LLNL-SCI-465-V5 (Orme 2004b).

Note: Image BF2301 is shown at 17.5kx magnification with scale bar 200nm in a) and image BF2306 is shown at a higher magnification value of 65kX and scale bar 200nm in b). The base-metal is at the top side of the image. From image a) it can be seen that the oxide varies in thickness. In image b) the oxide is approximately 30nm. The oxide, does not have light and dark regions typical of polycrystalline films and thus is likely amorphous (or polycrystalline on a scale too small to see at these magnifications).

Figure 11. Cross-sectional TEM images of autoclaved sample DEA1127, held for ~9-months in a 140C brine solution with NO_3/Cl ratio 0.5.

Both the 4-month and 9-month samples held in NO_3/Cl 0.05 environments, show considerable variation in their oxide surfaces. This is most apparent from the low-magnification images in Figure 9a and Figure 9b. In the $\sim 3\mu\text{m}$ region where the TEM images were obtained, the oxide thickness varies from 0--60nm. From the higher magnification images in Figure 9c and Figure 9d, the oxide appears less porous and more homogeneous at later times. The metal remains smooth in both cases. SEM analyses suggest that variation in oxide thickness is due to variation of Ni-rich oxides over the surface. This is supported by small spot Auger analysis (not shown) of sample DEA700, which show that the brighter, upraised regions had more nickel and less chromium than the darker regions, suggesting that the mottled appearance is due to a nickel-rich oxide that deposits in islands on the surface. From the SEM images it appears that at the earlier times small islands are distributed across the surface whereas at later times these partially coalesce creating larger regions of nickel-oxide as well as larger regions without this deposit. Auger depth profiles (not shown) for all metal constituents of Alloy 22 and the solution salts show that the surface is predominately composed of nickel, chromium and oxygen (aside from carbon silicon and aluminum contaminants). The surface contains no significant chloride

a)	b)
----	----



Source: Images from Charles Evans report C04J4575, MOL.20041101.0419

Note: The images are non-Q. a) Sample DEA1046 aged ~4-months. b) Sample DEA700 aged ~9-months. The Auger analysis sampled over an area of ~18μm x ~13μm.

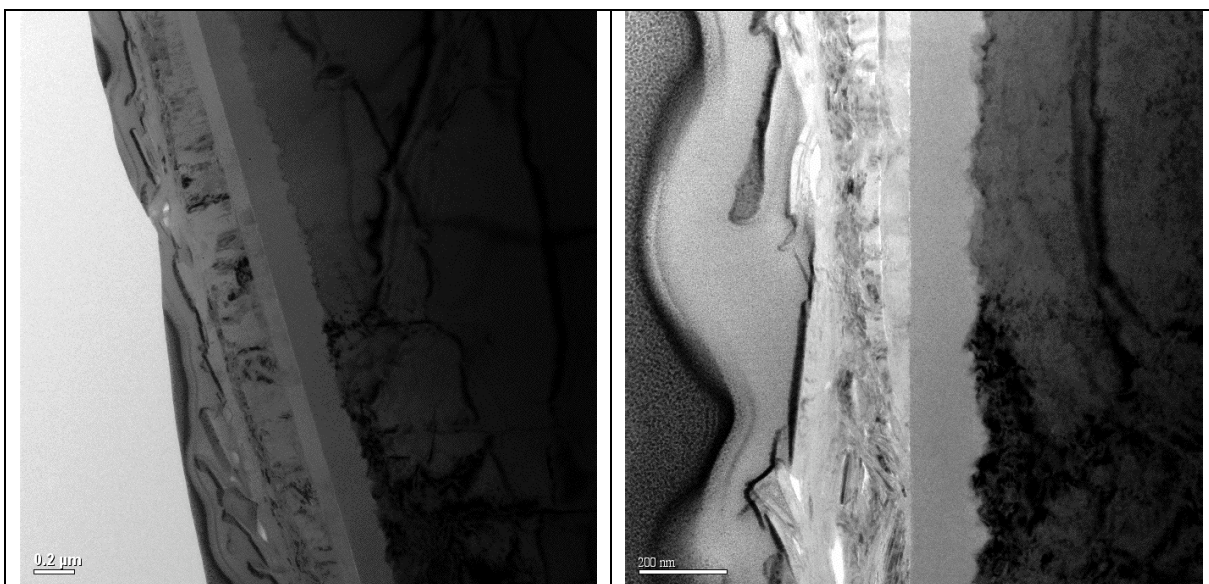
Figure 12. SEM images of surfaces where Auger depth profiling was performed.

At the higher nitrate to chloride ratio of 0.5, which is high enough to significantly reduce crevice corrosion, the oxide looks very similar to that at low ratios for these non-creviced specimens. The oxide is thinner but non-uniform in thickness varying from a few nanometers to ~30nm and is composed of approximately 75% nickel, 19% chromium, 5% iron and 2% molybdenum. Consistently, the corrosion rates at $\text{NO}_3^-/\text{Cl}^-$ ratios of 0.05 and 0.5 are approximately the same. This suggests that the low acid conditions of a creviced specimen are necessary to observe differences in corrosion rates due to $\text{NO}_3^-/\text{Cl}^-$ ratio in the range of 0.05 to 0.5.

In contrast to the fairly thin non-uniform oxide layer at 140°C, cross-sectional TEM images (Figure 14) show that a very thick (0.5μm) oxide has formed on the Alloy 22 surface in solutions with $[\text{NO}_3^-]/[\text{Cl}^-] = 0.3$ at the highest temperature tested, 220°C. It is clear from the ragged appearance of the base-metal that the metal has corroded and transformed into a stratified oxide. This oxide is more than 10 times thicker than the oxides formed at 140°C in solutions that bound this nitrate to chloride ratio, which suggests that temperature rather than $[\text{NO}_3^-]/[\text{Cl}^-]$ ratio is responsible for the dramatically different oxide formation.

a) Image BF2104.tif.

b) Image BF2106.tif

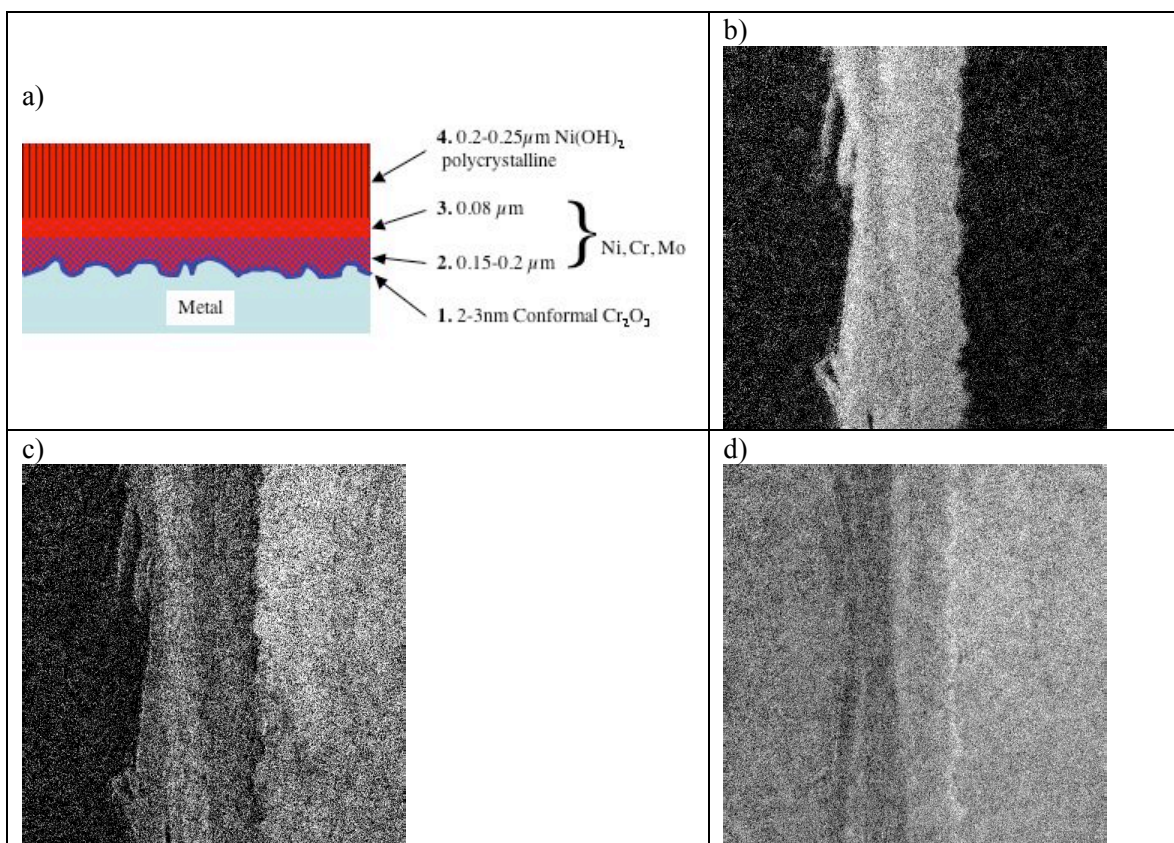


Source: Images from SN-LLNL-SCI-465-V5. (Orme 2004b)

Note: Image BF2104 (a) is shown at 8.8kx magnification with scale bar 0.2μm and image BF2106 (b) is shown at a higher magnification value of 17.5kX and scale bar 200nm. The metal is at the right side of the image. Three separate oxide layers can be seen between the partially fractured, dark Pd-Au sputtered layer and the base-metal. This is best seen in a) where the total oxide thickness varies from ~0.5μm-0.6μm over the imaged region.

Figure 13. Cross-sectional TEM images of autoclaved sample DEA686, held for ~9-months in a 220C brine solution with NO_3/Cl ratio 6.7.

The oxide has four distinct oxide layers within it. Three of the layers have different morphologies that can be seen in the bright field images. These are clearest in Figure 12a, which shows a homogeneously colored oxide nearest the jagged base-metal followed by a lighter, still uniform oxide that is ~0.08μm thick, and a thicker, ~0.2-0.25μm thick mottled layer. The mottled pattern is an indication that this outermost layer is polycrystalline. From the XPS studies the outer layer is identified as $\text{Ni}(\text{OH})_2$. The fourth layer is deduced from the oxygen, chromium, and nickel elemental maps in Figure 13. In particular the chromium map in 9d has an enriched chromium region at the base-metal boundary while the nickel map has a dark, denuded region. Together these data suggest that a thin, conformal chromium oxide layer (presumably Cr_2O_3) exists similar to what is found in passive film studies over a wide range of solution conditions. The four layers are labeled and shown schematically in figure 9a. From the elemental maps it is difficult to determine compositional differences between the layers labeled 2 and 3 in Figure 13a. It is clear that both of these layers contain chromium although the concentrations are lower than the bright line of conformal Cr_2O_3 in layer 1. The nickel elemental map also shows that layers 2 and 3 contain nickel at a level less than the $\text{Ni}(\text{OH})_2$ poly crystalline layer and more than the dark layer that we identify as Cr_2O_3 . This is supported by the Auger depth profile (Figure 14). These layers are likely a mixed oxide with nickel, chromium and perhaps molybdenum content.

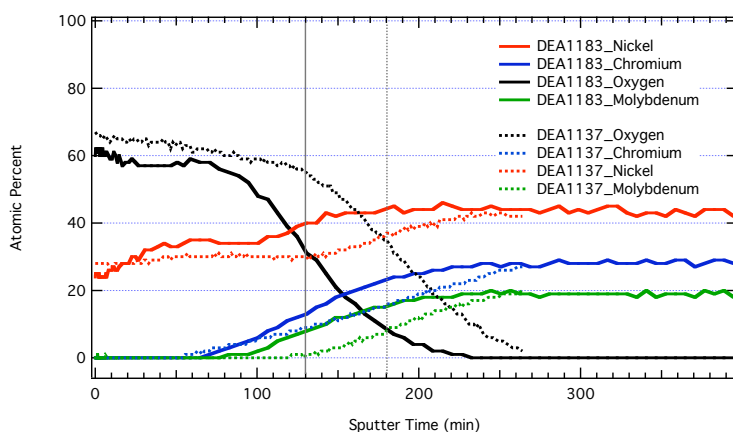


Source: Images are from SN-LLNL-SCI-465-V5 (Orme 2004b)

Note: The region and size scale are approximately the same as shown in Figure 12b.

Figure 14. The oxide composition of DEA686 is shown schematically in a). Energy electron loss spectroscopic maps provide b) oxygen, c) nickel, and d) chromium composition.

The XPS and Auger depth profile were used to compare the 4-month sample with the 9-month sample. From the Auger depth profile (Figure 14), the stratified layers are less evident than seen in the TEM images. This is because Auger electrons come from a range of depths and because surface roughness smears the interfaces. The 9-month samples have a thicker oxide than the 4-month samples as one would normally expect and the overall composition profile is similar for both time points. Both samples show the nickel-rich outer oxide with increased chromium in the oxide approaching the metal substrate. From XPS analysis of the surfaces, the samples are predominately nickel in the form of $\text{Ni}(\text{OH})_2$. Both samples show some iron (3-6%) in the nickel layer, very little molybdenum (<0.5%) and almost no tungsten (<0.1%). The Ni/Cr ratio is much higher (30 as compared to 7) at the later times presumably due to the thickening of the $\text{Ni}(\text{OH})_2$ layer with time. From XPS analysis (Table 4) the two samples aged in vapor had surface compositions that were almost the same for both times points and were most similar to the 4-month solution sample. In particular the Ni/Cr ratios were ~6. This either suggests that the $\text{Ni}(\text{OH})_2$ layer does not thicken to the same degree in vapor, or that Nickel at the oxide-solution interface preferentially leaches into solution which it can not do in the vapor phase.



Source: Data from Charles Evans report C04J4575, MOL.20041015.0104.

Note: The vertical lines show the approximate locations of the oxide-metal interfaces as determined by the full width at half maximum method. From the Auger profiles the sample aged ~4-months (solid curves) has a thinner oxide than the sample aged for longer times (dashed curves) as is expected. The data are normalized to 100% of elements detected but only nickel, chromium, molybdenum, and oxygen are plotted.

Figure 15. Auger depth profiles of sample DEA1183, aged ~4-months and DEA1137, aged ~9-months in 220 °C brine solution with $\text{NO}_3/\text{Cl} = 0.3125$.

In all cases, the data are consistent with a conformal chromium oxide layer at the metal oxide interface overlaid with $\text{Ni}(\text{OH})_2$ islands. The coverage and thickness of the $\text{Ni}(\text{OH})_2$ varies with environment and becomes 100's nanometers thick at the highest temperatures (220°C). Given that the corrosion rates do not depend on the whether the $\text{Ni}(\text{OH})_2$ completely covers the surface, we conclude that the chromium oxide layer is responsible for the low corrosion rates.

Implications to the General Corrosion Model

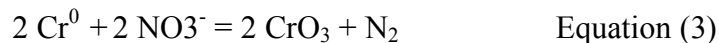
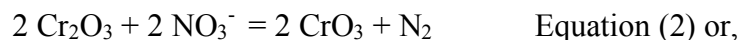
The program's current general corrosion model is dependent on temperature, but not on solution composition. The resulting rate equation relies on long-term weightloss data to derive the rate constant and short-term electrochemical data to derive the temperature dependence (because no temperature dependence was observed in the 60 and 90°C weightloss studies). Findings from the general corrosion studies highlighted here support this rate model. The new weight-loss corrosion data from this current study finds a temperature dependency (10 ± 3 kJ/mol) between the LTCTF measurement, which is consistent with 0kJ/mol and the short-term electrochemical tests, which find 25kJ/mol. Furthermore, general corrosion rates for Alloy 22 do not appear to be strongly dependent on the $\text{NO}_3:\text{Cl}$ ratio except at very high $\text{NO}_3:\text{Cl}$ (6.7). Both surface analyses and macroscopic rates are similar for $\text{NO}_3:\text{Cl}$ ratios of 0.05 and 0.5 at 140°C. Thick oxide layers and clear faceting of the metal interface resulting from corrosion at 220C and $\text{NO}_3:\text{Cl} = 0.3$ further support the model by showing that temperature is more important than the chemical environment for generalized corrosion in these not very acidic conditions. This is not the case for localized corrosion in which $\text{NO}_3:\text{Cl}$ above 0.2 have

been shown to inhibit corrosion. The effect of NO₃/Cl in acid solutions is further discussed in section 4.

Our data suggest that at very high NO₃:Cl ratios high temperature, NO₃⁻ appears to enhance general corrosion by enabling the oxidation of Cr metal to Cr(VI). This interpretation is based on two samples at NO₃:Cl = 6.7 and 160C and limited XPS analyses of surface Cr speciation . Further work is needed to determine if NO₃ contributes to Alloy 22 dissolution in concentrated solutions, because recent work shows that very concentrated brines with high NO₃:Cl solutions are stable to temperatures above 180°C (Carroll et al., 2004).

The role of the oxide film is to limit diffusion between the environment and the metal. In cases where the oxide is stable, the growth is a self-limiting process (i.e., as the film thickens, the diffusion across it slows, and the metal oxidizes at an ever-diminishing rate). In cases where the oxide is not thermodynamically stable, it is dissolving at the oxide–solution interface. As the oxide dissolves, the metal oxidizes at the metal–oxide interface. The system achieves a steady state with a particular oxide thickness when the oxide dissolution and the metal oxidation rates are balanced. Once sufficient metal has transferred to solution, the solution becomes saturated with respect to the oxide, and the driving force for dissolution at the oxide–solution interface stops. The findings of KTI Appendix N, is that Alloy 22 develops a chromium oxide barrier layer in the range of environments tested (NaCl and multi-ionic brines at pH values approximately 3 to 12). The oxide phases expressed are consistent with thermodynamically stable oxides in the passive region but given the low metal concentrations in solution, it is more likely that the oxides are kinetically stable, representing the second case. Thus, the low general corrosion rates measured in short-term tests are a reflection of the slow dissolution kinetics of chromium oxide and in particular, a chromium oxide in the 3+ oxidation state such as Cr₂O₃. It is possible that the thin water layer conditions of the vapor specimens can achieve a saturated solution state but further analysis would be needed to compare the predicted metal ion concentrations in solution with the measured weightloss.

In the high nitrate environment it appears that Cr₂O₃ either partially converts to CrO₃, or that CrO₃ forms directly from chromium in the base metal. For example, reactions such as:



result in the conversion of Cr(0) or Cr(III) to Cr(VI). And because CrO₃ is more soluble than Cr₂O₃, it dissolves faster leading to a higher corrosion rate. In most environments the corrosion rate reflects the dissolution of Cr₂O₃ (or other Cr(III) oxides) and from electrochemical tests the activation barrier for this process is 25kJ/mole. However in environments sufficiently oxidizing to form CrO₃, dissolution occurs by a different mechanism, which changes the prefactor, R₀, and the activation barrier E.

To summarize the autoclave studies, all environments tested had corrosion rates less than 0.25 microns per year even at 220°C. The oxides that formed on the surfaces were predominately Ni(II) oxides consistent with Ni(OH)₂. The oxides also contained chromium. Several samples showed evidence of stratification with a nickel oxide outer layer and a more chromium rich inner layer. For most samples the chromium was predominately in the 3+ oxidation state. In one of the environments (NO₃/Cl=0.3125) where a Cr(III) oxide formed, the corrosion rate was measured over a temperature range of 120-220°C. The activation barrier was measured to be of 8±8 kJ/mole, which is lower than the activation barrier measured in electrochemical tests (25kJ/mole). If all positive corrosion rates are used, independent of the solution type, an activation barrier of 10±3 kJ/mole is measured. The lower activation barriers are more consistent with the LTCTF data, which showed no temperature dependence. In sufficiently oxidizing conditions, Cr₂O₃ converts to the less stable CrO₃, which causes a higher corrosion rate. The activation barrier for this process was measured to be 49±25 kJ/mole, although more data points would be advised.

4. CORROSION RATES IN CREVICE SOLUTIONS

Alloy 22s high corrosion resistance over a broad range of environments is attributed to the passive film that develops at the metal interface. As established above, the oxide remains protective even at high temperatures and in high brine conditions. However the oxide film will dissolve in sufficiently aggressive environments. In occluded regions such as crevices and pits it is possible for chemistries to evolve that are not in equilibrium with the outside environment. Metal hydrolysis reactions within the crevice can result in low pH solutions that can evolve at the same time that oxygen is depleted due to limited diffusion through the thin solution layers. Whether the oxide fails under these low pH and low oxygen conditions depends on the temperature, pH, and the relative concentrations of anions (such as chloride) to inhibitors (such as nitrate or sulfate).

To determine the limits of passive film stability in acidic conditions mimicking crevices, we have measured corrosion rates (as determined by polarization resistance) at 60°C and 90°C, on a coarse ionic strength grid (1M, 4M NaCl), a coarse NO₃/Cl ratio grid (0.005, 0.05, 0.2, 0.5) and a fine acid concentration scale (Hydrochloric, Sulfuric, Oxalic, Nitric). Hydrochloric, Nitric and Sulfuric acids are possible from the in-drift chemistry and oxalic and sulfuric acids are potential by-products of microbial activity. The nitrate to chloride ratios were chosen to span the value (0.2) where inhibition is seen in creviced specimens and two salt concentrations were chosen to test whether breakdown is a sensitive function of chloride concentration. The results of the autoclave experiments suggesting that very high nitrate to chloride ratios (6.7) can lead to less stable oxide films was not anticipated when the test matrix was designed and thus the highest ratio tested was 0.5. These measurements use an automated titration system that steps through solution conditions, measuring the open circuit potential (OCP), the polarization resistance and performing impedance spectroscopy measurements. In this report we summarize the OCP and corrosion rate data (as derived from the polarization resistance).

The information obtained establishes pH and solution compositions where Alloy 22 dissolution is sustainable. The data establish the “critical crevice solution chemistry” for localized corrosion. If a crevice can evolve to and sustain “critical crevice solution chemistry” then the specimen will corrode conversely, if the environment is not sustainable, crevice corrosion will stop. The data also elucidate the inhibiting effect of nitrate and sulfate by correlating corrosion rate with open circuit potential and surface morphology. In particular, this data set suggests that nitrate is very oxidizing under low pH conditions; this may promote a stable oxide film that inhibits localized corrosion.

CONNECTION TO CREVICE CORROSION MODELS

Occluded environments are unavoidable on the waste package and, where they exist, it is possible for chemistries to evolve that are not in equilibrium with the bulk solution. In particular, the oxygen concentration, pO_2 is limited by diffusion through a thin solution layers and can become depleted within the crevice region. This causes electrical potential profile to develop due to the chemical differences between the inside and outside of the crevice. Once the potential drop spans the active/passive transition region, metal dissolution occurs and can initiate crevice corrosion (Xu and Pickering). Within the program, electrochemical testing of crevice specimens has established passive film failure as a function of *external* bulk solution concentrations whereas the results shown here establish the limiting *internal* solutions. The results are not directly comparable however for the purposes of discussion the localized corrosion model is briefly summarized.

The empirical formula for determining breakdown is determined by the relative values of the open circuit potential (E_{corr}) and the critical potential (E_{crit}). These values were determined for solutions in the range of pH 4 to 12. Within the model, corrosion initiates when $E_{corr} \geq E_{crit}$, where E_{crit} is defined as the repassivation potential, E_{rcrev} . The open circuit potential is a function of temperature (T), solution pH, chloride concentration and when nitrate is present, the NO_3/Cl ratio with functional dependencies as shown in equation 4.

$$E_{corr} = c_0 + c_1T + c_2pH + c_3[Cl] + c_4 \log[NO_3]/[Cl], \quad \text{Equation 4}$$

where $c_0 = 558 \pm 36 \text{ mV}$, $c_1 = 0.7 \pm 0.4 \text{ mV/C}$, $c_2 = -65 \pm 2 \text{ mV}$, $c_3 = 8 \pm 2 \text{ mV/molal}$, and when nitrate is present, $c_4 = 37 \pm 2 \text{ mV}$ otherwise this term is omitted.

The critical crevice potential in the absence of nitrate is given by:

$$E_{crev} = E_{0crev} = a_0 + a_1T + a_2pH + a_3[Cl] + a_4 \log[Cl], \quad \text{Equation 5}$$

where $a_0 = 214 \pm 46 \text{ mV}$, $a_1 = -3.7 \pm 0.5 \text{ mV/C}$, $a_2 = 25 \pm 6 \text{ mV}$, $a_3 = 252 \pm 54 \text{ mV/molal}$, and $a_4 = 1.4 \pm 0.5 \text{ mV}$. When nitrate is present $E_{crev} = E_{0crev} - \Delta E_{crev}^{NO_3}$ where $\Delta E_{crev}^{NO_3}$ is given by:

$$\Delta E_{crev}^{NO_3} = b_0 + b_1[NO_3] + b_2 \log[NO_3]/[Cl] \quad \text{Equation 6}$$

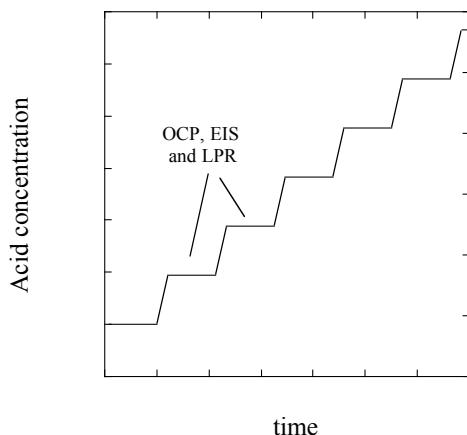
with $b_0 = 23 \pm 24$, $b_1 = 34 \pm 5$, and $b_2 = 750 \pm 95$.

For all equations listed above, concentrations are in molal (mol/Kg-H₂O) and temperature is in Celcius (BSC 2004a).

The open circuit potential obtained in the current data set can be directly compared to the predicted values for E_{corr} although the titration data have much lower pH values than those used to calculate the empirical coefficients. It will also be shown that sufficiently high NO₃/Cl ratios suppress an active/passive response and can be used to understand the inhibition of crevice corrosion in the context of the Pickering model.

METHODS: TITRATION EXPERIMENTS

We have developed a new titration method to test Alloy 22 passive film breakdown as a function of chloride, nitrate, sulfate, and oxylate concentrations over a wide range of acidity at 60 and 90°C. The technique is illustrated in Fig. 16.



Notes: During the periods of constant acid concentration, open circuit potential (OCP), electrochemical impedance spectroscopy (EIS) and linear polarization resistance (LPR) measurements are performed to characterize the corrosion properties of the Alloy.

Figure 16. Schematic of Acid Concentration as a Function of Time for a Representative Titration Experiment.

Initially, the Alloy 22 sample is immersed in a de-aerated, one-liter electrochemical cell filled with either 1 m or 4m sodium chloride. The initial pH varied from ~4-6. An open circuit potential (OCP) measurement is performed for 1.5 hours to condition the sample surface with the solution. This appears to be a sufficient conditioning period, because 3

day measurements found very little change after the first hour in acidic conditions. This wait time may be insufficient under neutral conditions and thus the OCP values for first couple data points in the titrations may be under estimated. Following the OCP measurement, electrochemical impedance spectroscopy (EIS) and three consecutive linear polarization resistance (LPR) measurements are used to characterize the corrosion rate. Upon completion of the LPR measurements, a programmable dual syringe pump is used to withdraw a precise volume of solution from the electrochemical cell and subsequently dispense a well-defined volume of acid (from an external reservoir) into the cell. In addition to acid, the external reservoir contains an equal amount of sodium chloride as the initial cell volume. Consequently, the amount of sodium chloride in the cell remains constant while the overall acid concentration increases. Once the syringe pump dispenses acid into the cell, an OCP measurement is once again performed followed by LPR. This process is repeated many times until the pH is well below zero.

Hydrochloric, sulfuric and nitric acid titrations were all performed in a constant sodium chloride solution of 1 and 4m while oxalic acid titration was performed in 0.125m sodium chloride due to precipitation at higher concentrations. The sodium chloride concentration remains fixed throughout the titration for pure sulfuric, oxalic and nitric titrations. However, the total chloride concentration varies when HCl is one of the titrants or when various NO₃/Cl and SO₄/Cl ratios are being maintained. The test matrix and corresponding sample identification is shown in Table 7.

Table 7. Test Matrix for the Titration Experiments

Sample ID	T C	Initial [NaCl] ¹	Acid	NO ₃ /Cl	SO ₄ /Cl
DEA1114	60	1	HCl	0	0
DEA661	60	1	H ₂ SO ₄	0	varies
DEA577	50	1	Oxalic	0	0
DEA1121	90	1	HCl	0	0
DEA1139	90	1	HNO ₃	varies	0
DEA1062	90	1	H ₂ SO ₄	0	varies
DEA1059	90	1	Oxalic	0	0
DEA671	90	4	HCl	0	0
DEA679	90	4	HNO ₃	varies	0
DEA678	90	4	H ₂ SO ₄	0	varies
DEA662	60	1	0.05 NO ₃ /Cl	0.05	0
DEA663	60	1	0.2 NO ₃ /Cl	0.2	0
DEA660	60	1	0.5 NO ₃ /Cl	0.5	0
DEA1113	90	1	0.005 NO ₃ /Cl	0.005	0
DEA1125	90	1	0.05 NO ₃ /Cl	0.05	0
DEA1124	90	1	0.2 NO ₃ /Cl	0.2	0
DEA514	90	1	0.5 NO ₃ /Cl	0.5	0
DEA677	90	4	0.05 NO ₃ /Cl	0.05	0
DEA676	90	4	0.2 NO ₃ /Cl	0.2	0
DEA670	90	4	0.5 NO ₃ /Cl	0.5	0

DEA668	60	1	0.1 SO ₄ /Cl	0	0.1
DEA688	60	1	0.5 SO ₄ /Cl	0	0.5
DEA669	60	1	1 SO ₄ /Cl	0	1
DEA664	90	1	0.1 SO ₄ /Cl	0	0.1
DEA682	90	1	0.5 SO ₄ /Cl	0	0.5
DEA665	90	1	1 SO ₄ /Cl	0	1

¹ Molal. This value remains fixed throughout the titration for pure sulfuric, oxalic and nitric titrations. However, the chloride concentration varies when HCl is one of the titrants as is the case for HCl and the various NO₃/Cl and SO₄/Cl ratios.

Note: Samples held at 50 or 60°C are shown with a grey background.

THE EFFECT OF ACID TYPE ON CORROSION

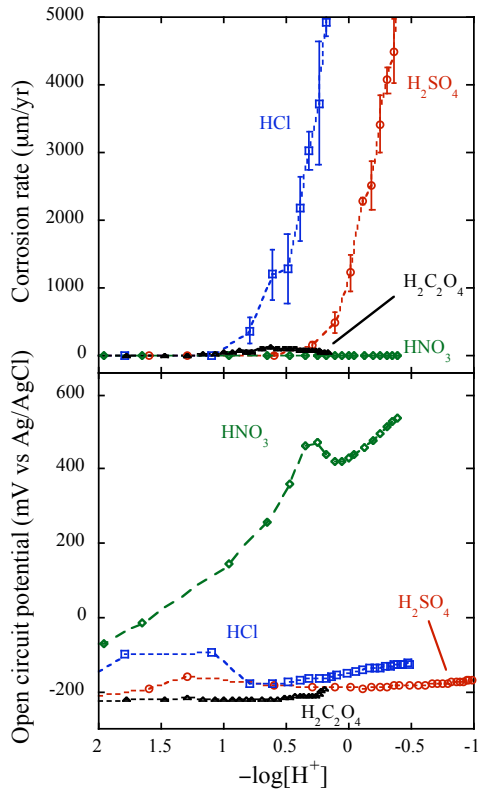
In this section we compare the critical acid concentrations that lead to the breakdown of the passive oxide film on Alloy 22 in hydrochloric (HCl), sulfuric (H₂SO₄), nitric (HNO₃), and oxalic (H₂C₂O₄) acids in sodium chloride (NaCl) containing environments at 60°C and 90°C.

Results and Discussion

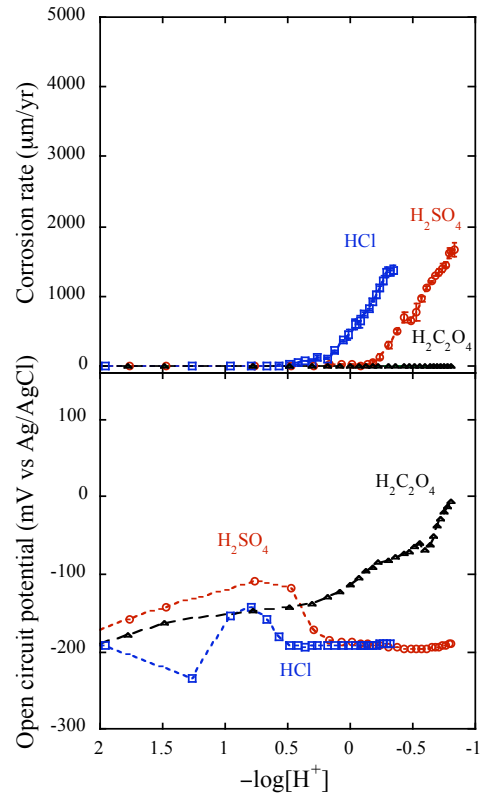
Figures 18-19 compare corrosion rates and open circuit potentials as a function of the negative logarithm of the hydrogen concentration for the different acids at 90°C in a 1m NaCl base, 60°C in a 1m NaCl base, and 90°C in a 4m NaCl base. For the purposes of these graphs, the acids are assumed to completely dissociate and are reported as the negative logarithm of the stoichiometric molality of Hydrogen ion solute component or –log m(H, St). This is a good assumption for hydrochloric and nitric acid because these are strong acids but is invalid for sulfuric and oxalic acid. Moreover the plots assume that sulfuric and oxalic acids contain two dissociated hydrogen ions. The true correspondence between acid concentrations and pH, which is a function of the hydrogen ion activity rather than concentration, requires geochemical modeling (which was outside the scope of this work).

The pH value where the corrosion rate rapidly increases marks the breakdown of the passive film of Alloy 22 and is the critical environment that leads to rapid corrosion. In this report we define the critical environment as the hydrogen concentration where the corrosion rate exceeds ~10 µm/year. In hydrochloric and sulfuric acid, the critical pH values at 90°C in 1m NaCl are 1 and 0.25, respectively. In more concentrated 4m salt solutions (figure 19) these both shift to higher values 1.5 and 2 for hydrochloric and sulfuric respectively. The breakdown of the passive film is also reflected in the open circuit potential curves where the OCP decreases at the onset of corrosion. No significant corrosion occurs for nitric acid and in the low pH range where the other solutions broke down the oxide film, the OCP steadily increases. Together these suggest that nitric acid acts as an oxidizer, which perfects the oxide film and raises the OCP into the passive region. Oxalic acid shows significant corrosion rates at a pH of 0.5, but the passive film does not completely breakdown as indicated by the lower corrosion rates and the higher OCP at low pH.

a)

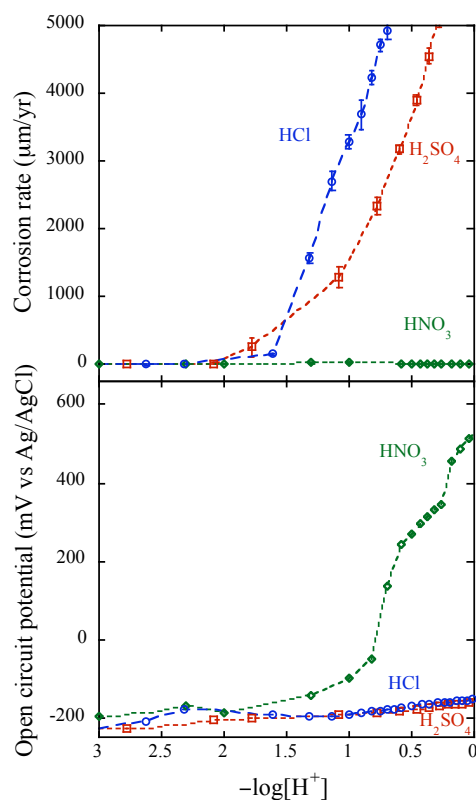


b)



Source: Orme 2004b.

Figure 17. Corrosion rates (top) and OCP (bottom) vs $-\log[H^+]$ (pH) for hydrochloric (HCl), sulfuric (H_2SO_4), nitric (HNO_3), and oxalic ($\text{H}_2\text{C}_2\text{O}_4$) acids at 90°C at left and for HCl, H_2SO_4 and $\text{H}_2\text{C}_2\text{O}_4$ acids at 60°C at right.



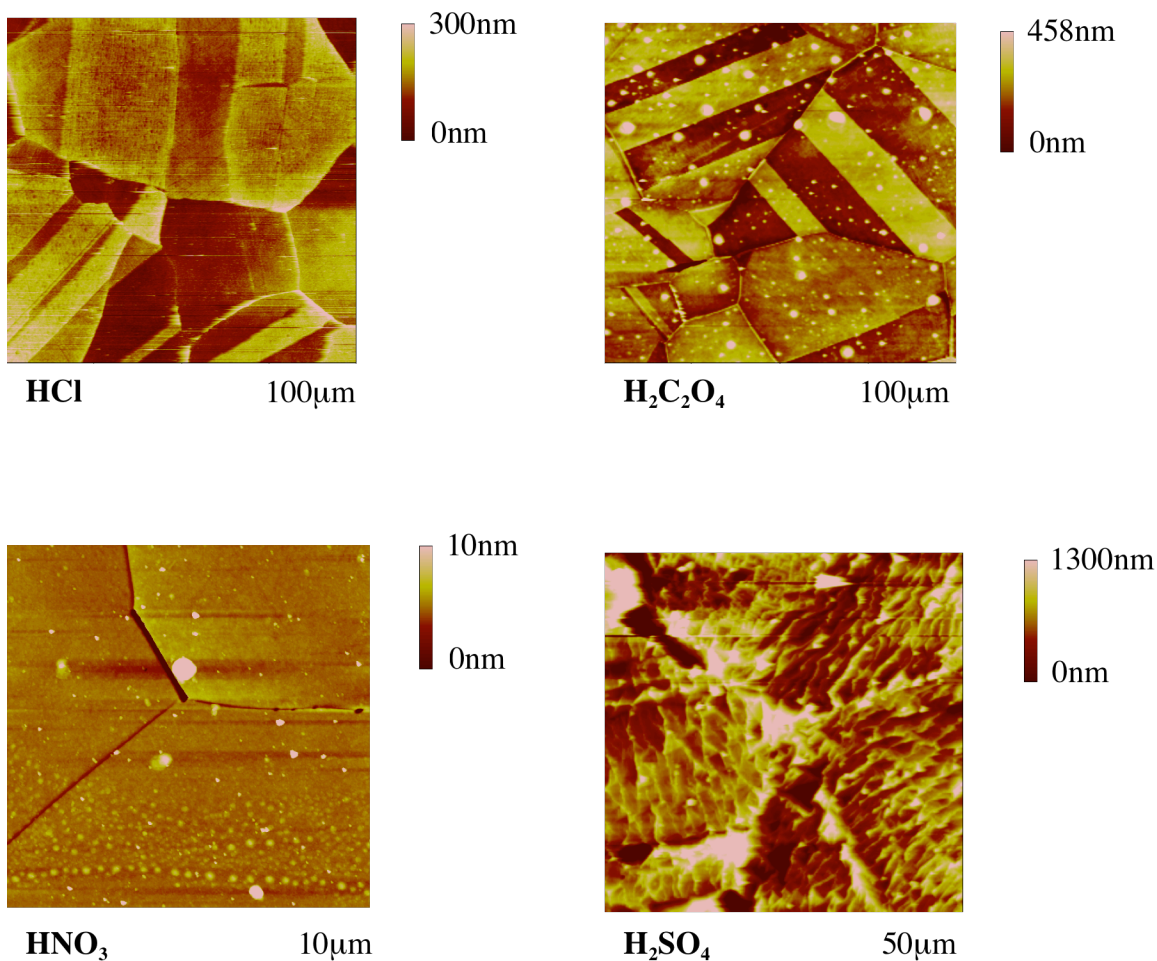
Source: Orme 2004b.

Figure 18. Corrosion rates (top) and OCP (bottom) vs $-\log[H^+]$ for HCl, H_2SO_4 and HNO_3 acids at 90°C in 4M NaCl.

The onset of crevice corrosion is strongly dependent on solution composition and is not a sole function of the acidity of the solution. The titration experiments show that nitrate in chloride solutions strongly inhibits corrosion as compared to pure chloride and chloride plus sulfate solutions. Note that nitric acid titrations were not performed at 60°C because no significant corrosion occurred at 90°C . Dissolved sulfate also appears to inhibit the corrosion as is illustrated by the lower $-\log[H^+]$ required to breakdown the passive film compared to the pure chloride solutions. The ability of sulfate to protect the passive film is smaller than reported here, because preliminary geochemical calculations (not shown) suggest that $-\log[H^+]$ required for passive film breakdown is about 0.45 units higher than shown in Figures 17-18. Oxalate plus chloride also appears to inhibit corrosion rates compared to pure chloride. However, the lower corrosion rates may be due to the 10 times lower chloride concentrations in the oxalic acid experiments than in the sulfuric and nitric acid titration experiments.

Atomic force microscope images of the surface morphology following titration experiments clearly indicate that the mode of metal dissolution differs in the different acid types. Samples exposed to titrations in hydrochloric and oxalic acids demonstrate similar modes of corrosion attack, in which preferential etching occurs depending on the orientation of the grain. Nitric acid titrations lead to mild intergranular attack and sulfuric acid environments show preferential etching at step edges. The micrographs indicate that specific atomic sites on the metal surface have higher dissolution rates than others in these acid environments. Overall this leads to a roughening of the surfaces and in particular, preferential grain etching (hydrochloric and oxalic) leads to large depressed regions suggestive of shallow pits 200-500nm deep and 10's of microns wide whereas intergranular etching (nitric) leads to thin narrow crevices. In some environments these geometries may be sufficiently occluded to allow chemical perturbations that initiate localized corrosion. For example, the higher corrosion rates at the grain boundaries observed in nitric acid may be caused when nitrate, which is consumed during metal oxidation, is not replenished within the crevice due to geometrical constraints on the diffusion.

The morphology observed in sulfuric acid is suggestive of a step-pinning mechanism that leads to slower dissolution of specific steps orientations. Each of the metal grains in the image has fluctuating steps that are approximately aligned in one orientation. Moreover, the steps have a scalloped appearance that often occurs when adsorbates impede the local motion of the step, eventually leading to the bunching of steps. Steps that do not have the proper chemistry, shape or size to allow adsorbate binding will move (dissolve) unimpeded resulting in a morphology that is dictated by the slower moving pinned steps. In the case of sulfuric acid, this suggests that step-specific sulfate binding plays a role in the inhibitory effect.



Source: Orme 2004a.

Note: The length of the edge is given below the image and the z-scale is shown at the right. The individual metal grains etch at different rates in HCl and H₂C₂O₄ resulting in a surface relief with the slowly etching metal grains upraised (light) relative to the faster etching grains (dark). In HNO₃, the metal grains etch at similar rates, but the grain boundaries etch faster and are therefore dark. In H₂SO₄, the metal grains are more difficult to discern but preferred step directions are apparent that change from grain to grain.

Figure 19. Atomic force microscopy (AFM) images of the surface morphology of Alloy 22 after titration experiments at 90°C in 1molal NaCl for HCl, H₂SO₄ and HNO₃ and 1/8 molal NaCl for H₂C₂O₄.

Table 8. Summary of Critical Environments

	Critical $-\text{Log}[\text{H}^+]$ in 1 molal NaCl at 90°C	Critical $-\text{Log}[\text{H}^+]$ in 4 molal NaCl at 90°C	Critical $-\text{Log}[\text{H}^+]$ in 1 molal NaCl at 60°C	Mechanism of breakdown
Hydrochloric (HCl)	1.0	1.5	0.0	Preferential grain etching

Sulfuric (H₂SO₄)	$0.25 + (0.3)^1 + (0.15)^2$	$2.0 + (0.3)^1 + (0.15)^2$	$-0.25 + (0.3)^1 + (0.15)^2$	Preferential step etching
Nitric (HNO₃)	No film breakdown	No film breakdown	No film breakdown	Mild Intergranular attack
Oxalic (H₂C₂O₄)	$0.5^3 + (0.3)^1$	N/A	No film breakdown ^{3,4}	Preferential grain etching

¹ Correction to account for the fact that H₂SO₄ and H₂C₂O₄ do not dissociate into 2 free hydrogens but rather are closer to one.

² Approximate correction to account for the fact that H₂SO₄ does not dissociate into 1 free hydrogen. This value varies from -0.1 to +0.15 in preliminary calculations that do not account for the changes in the activity coefficient due to the salt background.

³ Background salt solution is 0.125 molal.

³ Temperature is 50C.

THE CORROSION INHIBITING EFFECTS OF NITRATES AND SULFATES ON ALLOY 22 IN ACIDIC ENVIRONMENTS

We further investigated the inhibiting effects of nitrates and sulfates in crevice environments for ratios NO₃ to Cl (0.005 , 0.05, 0.2 and 0.5) (Figure 20-21) and for ratios of SO₄ to Cl (0.1 and 1) in sodium chloride solutions (Figure 23) at 60°C and 90°C using the same titration method. The effect of higher salt concentrations is considered for the nitrate study (1m and 4m NaCl). The goal of this research is to determine the critical NO₃:Cl and SO₄:Cl needed to maintain the passive film in a crevice environment, and to understand the physical mechanism of the inhibition process and breakdown.

Results and Discussion

Table 9. Summary of Critical Environments for Nitrate and Chloride Containing Solutions defined by the stoichiometric molal value of the Hydrogen ion $-\log m(\text{H}, \text{St})$ that causes Corrosion rates of $\sim 10\mu\text{m}/\text{year}$.

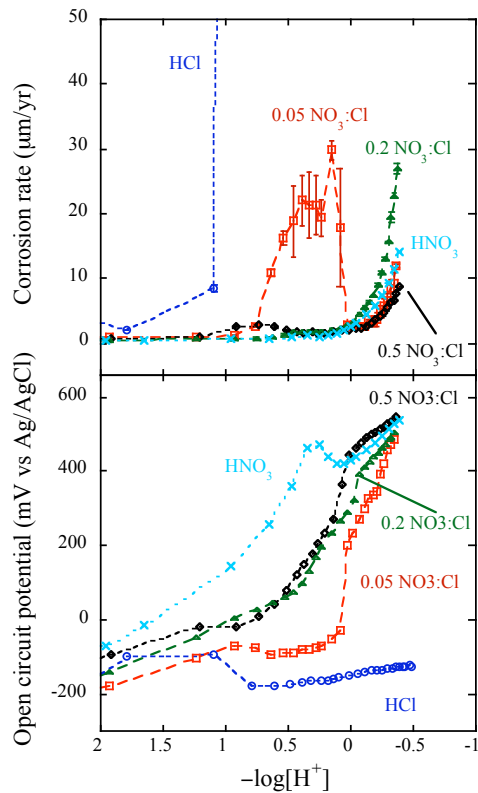
	Nitrate to Chloride Ratio				
	0	0.005	0.05	0.2	0.5
60°C, 1m NaCl	0.6	NA	-0.3	-0.4	-0.5
90°C, 1m NaCl	0.7	-0.2 ¹	-0.4 ¹	-0.3	-0.2
90°C, 4m NaCl	2.0	NA	0.1	0.2	0.0

¹ Chosen from the transpassive not the transient region of the curve.

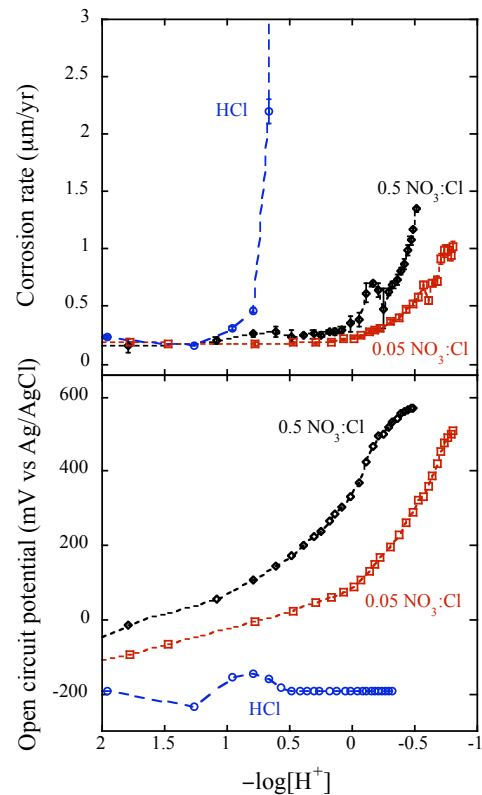
As summarized in Table 9, nitrate is a to be a very effective inhibitor of localized corrosion as is shown by the increased acidity required to breakdown the passive film in nitrate plus chloride solutions over chloride solutions alone (about 10 times more H⁺ at 60 and 90°C in 1 m NaCl solutions and 100 times more H⁺ at 90°C in 4 molal solutions). This implies that 10 to 100 times more hydrolysis of the metal is required to breakdown the passive film in the presence of nitrate. The ability of nitrate to stabilize the passive

film also depends on the relative ratio of NO_3 to Cl and temperature. In 90°C 1 and 4 molal NaCl solutions with $\text{NO}_3:\text{Cl} = 0.05$, there is a region reminiscent of an active passive transition where the corrosion rates increase then decrease until the critical $-\log[\text{H}^+]$ is reached. Presumably this represents restabilization of the passive film even at these low $\text{NO}_3:\text{Cl}$ ratios. In the lower salt concentration this occurs even with ratios as low as 0.005 (figure 22). The effect of NO_3 on passive film stability appears to reach a plateau above $\text{NO}_3:\text{Cl} = 0.2$, where higher ratios do not improve the performance of the passive film. Nitrate may be a more effective inhibitor of corrosion at lower temperatures, because we do not observe this transition in high to low corrosion rates at $\text{NO}_3:\text{Cl} = 0.05$ at 60°C .

a)

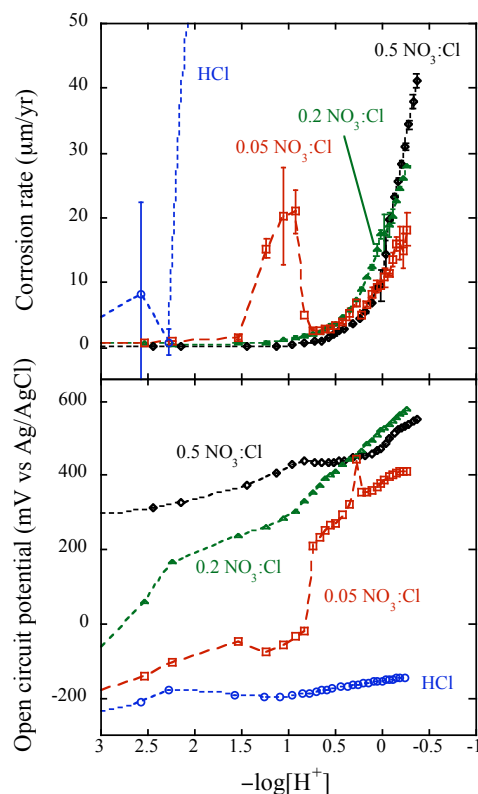


b)



Source: Orme 2004b.

Figure 20. Corrosion rates (top) and OCP (bottom) vs. $-\log[\text{H}^+]$ (pH) for hydrochloric (HCl) and nitric (HNO_3) acids and ratios of $\text{NO}_3:\text{Cl}$ of a) 0.5, 0.2 and 0.05 at 90°C and (b) 0.5 and 0.05 at 60°C .



Source: Orme 2004b.

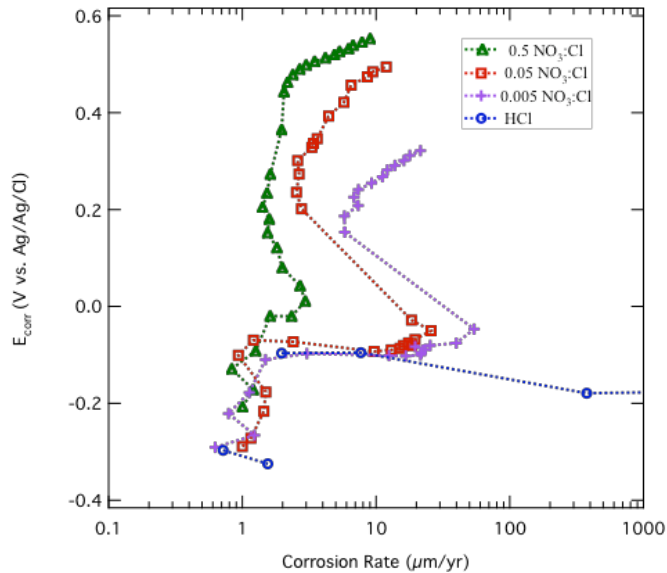
Figure 21. Corrosion rates (top) and OCP (bottom) vs. $-\log[H^+]$ (pH) HCl and ratios of $\text{NO}_3:\text{Cl}$ of 0.5, 0.2 and 0.05 at 90°C in an initial base of 4m NaCl.

The correlation between higher OCP and higher $\text{NO}_3:\text{Cl}$ also supports the interpretation that nitrate oxidizes Alloy 22 and stabilizes the passive film (Figures 20 and 21).

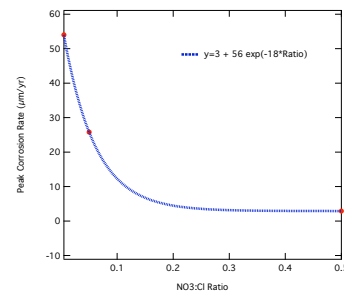
In the absence of nitrate, the OCP during hydrochloric titration is constant and negative and the passive film breaks down at relatively high pH values ($-\log[H^+]$ near 1 in 1 molal NaCl and near 2 in 4 molal NaCl at 90°C). By contrast, with a little nitrate ($\text{NO}_3:\text{Cl}=0.5$), the OCP is slightly higher than pure hydrochloric until the oxide film has repassivated but then rapidly approach the much higher OCP values of a pure nitrate system and at the same time the corrosion rates drop to a minimal level. The relationship between OCP and corrosion rate is further demonstrated in Figure 22. For all ratios of $\text{NO}_3:\text{Cl}$, the OCP rises with increasing acid concentration. Consequently, the Alloy passes through a region reminiscent of an active to passive transition at approximately 0mV versus Ag/AgCl. In this region the peak corrosion rates are a sensitive function of the $\text{NO}_3:\text{Cl}$ ratio decaying exponentially with ratio (Figure 22b). Once the acid concentration increases to a critical value (500mV for $\text{NO}_3:\text{Cl} = 0.5$, 300mV for $\text{NO}_3:\text{Cl}$

= 0.05 and 200mV for $\text{NO}_3:\text{Cl} = 0.005$), a transpassive-like corrosion rate dominates. Higher nitrate to chloride ratios move this transpassive behavior to higher potentials following a power law, with the breakdown potential increasing as the ratio to the 1/3 power. (Figure 22c).

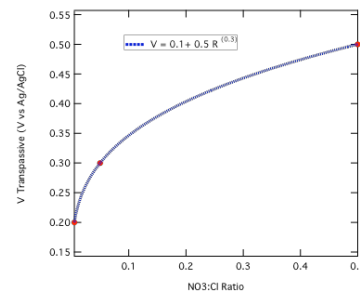
a)



b)



c)



Source: Orme 2004b.

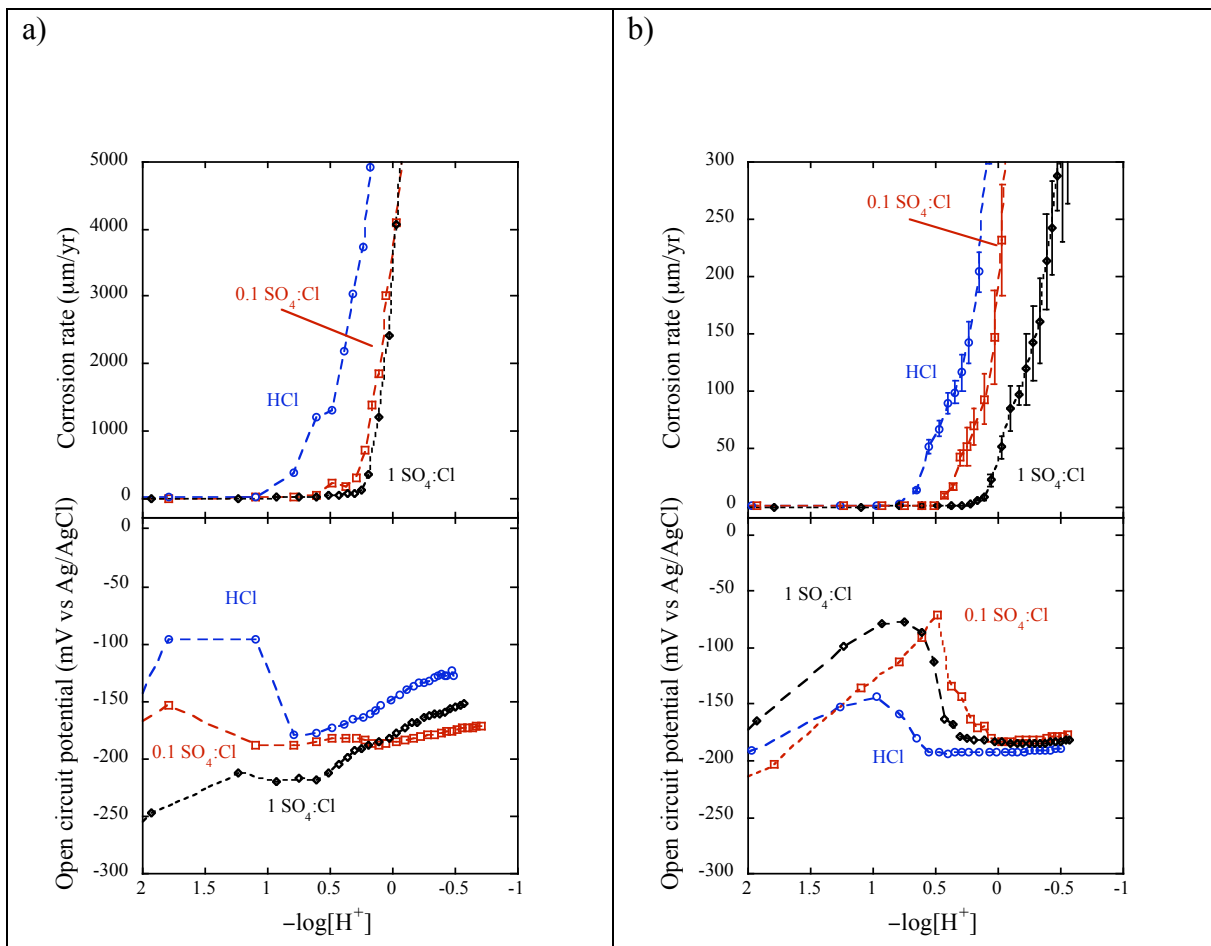
Note: Two points, (-0.024V, 17.2μm/yr) and (-0.026V, 3.9μm/yr) were removed from the 0.005 NO₃/Cl curve in figure 22a so that the curves did not overlap as much. In b) the peak corrosion rate versus the NO₃:Cl ratio can be fit with an exponential function, $\text{PeakCorrosionRate} = 3 + \exp(-18 \cdot \text{Ratio})$. In c) the break down potential where transpassive dissolution occurs, has a power law dependence on the nitrate to chloride ratio, $V_{\text{trans}} = 0.1 + 0.5 \cdot \text{Ratio}^{(0.3)}$.

Figure 22. Corrosion rates vs. OCP for HCl and ratios of NO₃:Cl of 0.5, 0.05 and 0.005 during acid titration experiments at 90°C with initial salt concentration of 1m NaCl.

From Figures 22, the critical NO₃ to Cl ratio for significant corrosion rates (and consequently crevice corrosion) in 1m NaCl at 90°C is between 0.05 and 0.5. This compares well with tests done at LLNL on actual crevice specimens where it is found that ratios greater than 0.2 do not crevice corrode. At 60°C, the corrosion rates are extremely low and the OCP values increase rapidly to the passive region. Consequently, no critical crevice ratio exists at 60°C for the ratios tested.

The corrosion inhibition effects of sulfates is much more subtle than in the case of nitrates. The effect is an overall shift in the critical $-\log[\text{H}^+]$ for passive film breakdown (Figure 29). In 1m NaCl at 90°C, the critical $-\log[\text{H}^+]$ for breakdown shifts from a value of 1 for HCl to about 0.4 for SO₄:Cl = 0.1 and 1 at 90°C and about 0.4 for SO₄:Cl = 0.1

and 0.0 for $\text{SO}_4:\text{Cl} = 1$ at 60°C . Critical $-\log[\text{H}^+]$ values for all SO_4 ratios in the tested environments are summarized in Table 1. Correcting the plots for the dissociation of sulfuric acid would increase the $-\log[\text{H}^+]$ to a value near 0.65 at 90°C and 0.65 to 0.25 at 60°C for sulfate containing NaCl brines (see above), indicating a very small effect of SO_4 on localized corrosion. Thus sulfate does not appear to oxidize Alloy 22 and preserve the passive film as does nitrate. This is supported by the negative OCP values for the sulfate plus chloride solutions.



Source: Orme 2004b.

Figure 23. Corrosion rates (top) and OCP (bottom) vs. $-\log[\text{H}^+]$ (pH) HCl and ratios of $\text{SO}_4:\text{Cl}$ of 1 and 0.1. in 1M NaCl at a) 90°C and b) 60°C .

Table 10. Critical $-\log[\text{H}^+]$ values for passive film breakdown for $\text{SO}_4:\text{Cl}$ ratios of 1:1 and 1:10 for 60°C and 90°C

	Critical $-\log[\text{H}^+]$ in 1 molal NaCl at 90°C	Critical $-\log[\text{H}^+]$ in 1 molal NaCl at 60°C
--	--	--

Hydrochloric (HCl)	1.0	0.75
1:10 SO ₄ :Cl	0.4	0.4
1:1 SO ₄ :Cl	0.38	0.0

IMPLICATIONS TO ALLOY 22 CORROSION AT YUCCA MOUNTAIN

In summary, the breakdown of the passive film of Alloy 22 occurs for HCl and H₂SO₄ in all environments tested and the critical pH for breakdown is a function of the temperature and molality of NaCl (Table 8). Oxalic acid begins to break down the passive film at 90°C but shows very little corrosion at 50°C where by-products of microbial activity might be expected. The chloride concentration used in this study is only 0.125 molal which corresponds to a very dilute seepage water that had undergone a minimal amount of evaporation. However, in more concentrated brines, NaCl will precipitate out of solution due to its low solubility in oxalic acid. The data show that no corrosion is expected from oxalic acid under repository conditions. Nitric acid does not breakdown the passive film of Alloy 22 in any of the tested environments.

Images show that the dissolution rates in HCl and oxalic are a function of grain orientation. The mechanism for corrosion for HNO₃ is mild intergranular attack. This may be caused by nitrate depletion from the crevice-like geometry. The morphology of the stepped surfaces in H₂SO₄ suggests that sulfates may interact with the Alloy 22 surface by site-specific interactions at surface steps.

This work clearly shows that in a crevice environment, nitrate effectively inhibits localized corrosion by raising the open circuit potential and passivating the surface. This can occur through coupled partial reactions such as,



and



which oxidize the chromium, ultimately converting it to Cr₂O₃. There are several reduced states of nitrate (NO₂⁻, N₂, NO, NO₂, NH₃) making many possible nitrate reactions. At this time, it is not possible to say if the increased stabilization is due to the formation of a thicker passivated film, or if it is due to a change in the structure or defect density within the film. However, in milder conditions (pH ~3) the passive oxide was shown to thin slightly as the potential increased within the passive region thus it is more likely that nitrate (which increases the OCP) acts to improve the quality of the oxide film rather than thickening it. Increased nitrate to chloride ratio has two positive effects that reduce the likelihood of crevice corrosion: it moves the breakdown potential to higher potentials

$\sim E_{trans} \propto \frac{[NO_3]^{0.3}}{[Cl]}$ (in the range tested); and NO₃:Cl exponentially, reduces corrosive currents before transpassive dissolution. The inhibitory effects of nitrate solutions

supports the localized corrosion model, in that it describes Alloy 22 corrosion in terms of nitrate to chloride ratio as shown in Equations 4-6. However, the details differ. In particular the interpretation that an increased E_{corr} corresponds to a more corrosion resistant oxide film is not captured by the localized corrosion model, where higher E_{corr} without a concomitant rise in the E_{rcrev} increases the likelihood of crevice corrosion.

To get a sense of how the localized corrosion model described by Equations 4-6 can be compared with the results of the titration model we plot one case with $\text{NO}_3:\text{Cl}$ ratio of 0.5, temperature 60°C , and 1molal NaCl initial solution (Figure 24). Comparing E_{corr} from the model (equation 4 in solid black) with the measured value (dotted grey) shows that the model is significantly higher at all acid concentrations, which is a conservative stance. E_{rcrev} (equation 5-6 in blue) is not monotonic in acid concentration because the $\text{NO}_3:\text{Cl}$ ratio is constant which means that the NO_3 concentration is increasing as the acid is increased. The difference between E_{corr} and E_{rcrev} is plotted in red, anywhere this curve is positive, crevice corrosion can initiate and the corrosion rate is set to $127 \mu\text{m}/\text{year}$. By comparison the largest measured corrosion rate (from the titration experiments) is $1.3 \mu\text{m}/\text{year}$ and this occurs at the lowest pH value (green trace). The difficulty with this comparison is that the model is based on bulk solution values and unknown crevice solutions whereas the titration experiments measure corrosion rates in bulk solutions that mimic crevice solutions. The YMP localized corrosion model suggests that a bulk solution with a $-\text{Log}[\text{H}^+]$ value of ~ 4.5 leads to a $-\text{Log}[\text{H}^+]$ value of less than -0.6 within the crevice (because this is where the oxide film breaks down). This implies that a crevice must be able to sustain a concentration gradient where the internal and external solutions differ by 5 orders in magnitude. Moreover, for this $\text{NO}_3:\text{Cl}$ ratio and temperature, there are no transient regions where high currents develop before transpassive dissolution. Thus if the $\text{NO}_3:\text{Cl}$ of 0.5 is sustained within the crevice it is unclear how crevice corrosion would initiate to drive the internal chemistry to the high acid concentrations required to break down the oxide. This reasoning suggests that the model is overly conservative and can be improved by considering sustainable concentration gradients in crevice geometries.

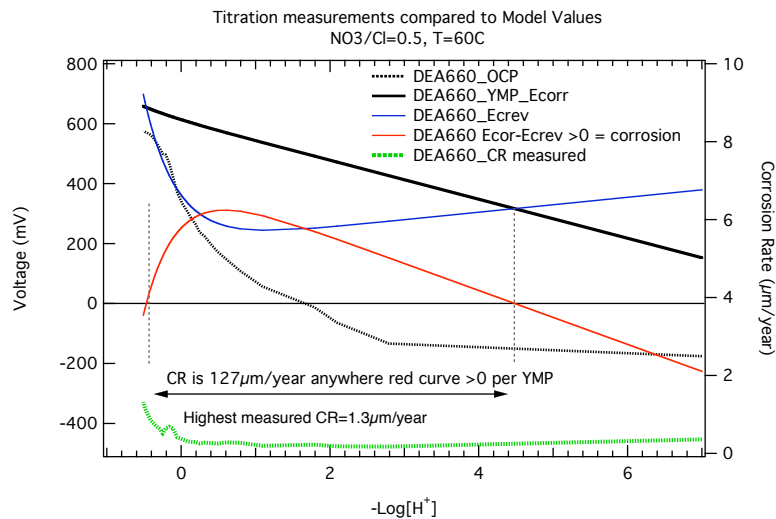


Figure 24. Titration Measurements Compared with the Localized Corrosion Model for $\text{NO}_3:\text{Cl}$ of 0.5, $T=60^\circ\text{C}$, and 1 Molal Initial NaCl solution.

The inhibitory effects of nitrate are important because they indicate that nitrate present in evaporating seepage water will mitigate any localized corrosion. Even at low $\text{NO}_3:\text{Cl}$ ratios of 0.05 at 60 and 90°C , these titration experiments indicate that initial corrosion sites will be repassivated. And at $\text{NO}_3:\text{Cl} \geq 0.2$, nitrate will effectively stabilize the passive film. However, because nitrate is depleted through reactions such as shown in equation 8, the sustainability of these reactions within a crevice will depend upon effective coupling with the environment. Nitrate is the most effective inhibitor found in evaporating seepage water. Although sulfate may also be present, this study shows that it does not stabilize the passive film to the same extent as nitrate. This should not be a concern, because both sulfate and nitrate are present in the evaporating seepage waters.

5. ACKNOWLEDGEMENTS

This work was performed under the auspices of the U.S. Department of Energy by the University of California, Lawrence Livermore National Laboratory under Contract No. W-7405-Eng-48.

6. REFERENCES

Documents Cited

BSC (Bechtel SAIC Company), 2004a. Waste Package and Drip Shield Corrosion in *Yucca Mountain Repository Safety Analysis Report DOE/RW-XXX cr_sar_234.doc* 2.3.6-36 Rev.00, Draft A, Las Vegas, Nevada.

BSC (Bechtel SAIC Company), 2004b. General Corrosion and Localized Corrosion of Waste Package Outer Barrier, ANL-EBS-MD-000003, Las Vegas, Nevada.

BSC (Bechtel SAIC Company), 2004c. Appendix N: Waste package and drip shield Materials: Passive film characteristics, growth, and stability, Las Vegas, Nevada.

Carroll, S., Alai, M., Craig, L., Gdowski, G., Hailey, P., Nguyen, Q. A., Rard, J., Staggs, K., Sutton, M., Wolery (2004) Chemical Environment at Waste Package Surfaces in a High-Level Radioactive Waste Repository, Lawrence Livermore National Laboratory, UCRL-TR-207919

Farmer, J. C., McCright, R. D., Gdowski, G. E., Wang, F., Summers, T. S. E., P., Bedrossian, Horn, J. M., Lian, T., Estill, J. C. (2000) A. Lingenfelter and W. Haalsey, Transportation, Storage, and Disposal of Radioactive Materials 2000, PVP-ASME, **408**, p. 53, New York, NY.

LLNL (Lawrence Livermore National Laboratory) 2004a. Acceptance Report for Scientific Investigations, for Charles Evans & Associates, X-Ray Photoelectron Spectroscopy (XPS) Surface Analysis Report. EAG Number: C04J4575. PO BA004609, REL 52456. ACC: MOL.20041015.0104.

LLNL (Lawrence Livermore National Laboratory) 2004b. Acceptance Report for Scientific Investigations, for Charles Evans & Associates, Auger Electron Spectroscopy (AES) Surface Analysis Report. EAG Number: C04J4575. PO BA004609, REL 52456. ACC: MOL.20041101.0419.

LLNL (Lawrence Livermore National Laboratory) 2004c. Acceptance Report for Scientific Investigations, for Charles Evans & Associates, X-Ray Photoelectron Spectroscopy (XPS) Surface Analysis Report. EAG Number: C04J0890. PO BA004609, REL 46868. ACC: MOL.20041007.0076.

Orme, C. 2004a. Oxide Characterization. Scientific Notebook SN-LLNL-SCI-465-V4. ACC: **MOL# not yet assigned 11/20/04.**

Orme, C. 2004b. Oxide Characterization. Scientific Notebook SN-LLNL-SCI-465-V5. ACC: **MOL# not yet assigned 11/20/04.**

Wong (L. L., Estill, J. C., Fix, D. V., Rebak, R. B. (2003a) General and localized corrosion behavior of titanium grades 2, 16, and 12 in simulated concentrated ground waters. American Society of Mechanical Engineers Pressure Vessels and Piping Conference.

Wong, L. L., Fix, D. V., Estill, J. C., McCright, R. D., Rebak, R. B. (2003b) Characterization of the corrosion behavior of alloy 22 after five years immersion in multi-ionic solutions.

Wong, L. L., Lian, T., Fix, D. V., Sutton M., Rebak, R. B. (2003c) Surface analysis of Alloy 22 coupons exposed for five years to concentrated ground waters. NACE International, Corrosion Conference.

Xu, Y. and Pickering, H. W. "The Initial Potential and Current Distributions of the Crevice Corrosion Process," J. Electrochemical Society, Vol. 140, No. 3, 1993, pp. 658-668.

Codes, Standards, and Regulations

ASTM G 59-97. 1998. *Standard Test Method for Conducting Potentiodynamic Polarization Resistance Measurements*. West Conshohocken, Pennsylvania: American Society for Testing and Materials. TIC: 249897.

ASTM G 102-89 (Reapproved 1999) 1989. *Standard Practice for Calculation of Corrosion Rates and Related Information from Electrochemical Measurements*. West Conshohocken, Pennsylvania: American Society for Testing and Materials. TIC: 249897.

ASTM G1-90 (Reapproved 1999) *Standard Practice for Preparing, Cleaning, and Evaluating Corrosion Test Specimens*. West Conshohocken, Pennsylvania: American Society for Testing and Materials. TIC 238771

N.5.3 Data, Listed by Data Tracking Number

LL030412512251.057 LTCTF Corrosion Rate Calculations for Five-Year Exposed Alloy C22 Specimens Cleaned Under TIP-CM-51. Submittal date: 5/28/03.

LL040502512251.099 Weight Loss Measurements and Weight Loss Corrosion Rates from Alloy 22 Foil Specimens. Submittal date: 04/20/2004.

LL040907112251.122 Weight Loss Measurements and Weight Loss Corrosion Rates from Alloy 22 Foil Specimens. Submittal date: 10/20/2004.